TURKGEO

TURKISH JOURNAL OF GEOSCIENCES

e-ISSN 2717-7696

OPEN ACCESS

dergipark.org.tr/tr/pub/turkgeo
turkgeosciences@gmail.com

TURKGEO, March/2025
Volume: 5 - Issue: 1

About The Journal

Turkish Journal of Geosciences is a multi-disciplinary open-access journal aimed to publish peer-reviewed original research and review articles covering all aspects of geosciences. The journal includes a wide scope of information on scientific and technical advances in all areas related to geosciences and indexed in international indices and databases that publish studies on earth sciences.

Aim and Scope

TURKGEO Journal has the following aim and scopes;

Aim of TURKGEO

- TURKGEO aims to promote the theory and practice from the integration of instruments, methodologies, and technologies and their respective uses in the environmental and other natural sciences.
- TURKGEO aims to provide a widely accessible discussion environment that will strengthen and accelerate the exchange of knowledge and experience among scientists, researchers, engineers and other implementers involved in the subject directly or indirectly.

Scope of TURKGEO

- Earth and Environmental Sciences Applications
- Geographic Information Systems
- Remote Sensing
- Photogrammetry
- Geostatistics
- GPS/GNSS
- RADAR/SAR/LIDAR and Laser Scanning
- Spatial Data Infrastructure
- Spatial Decision Support Systems
- Climate Change
- Geology
- Geomorphology
- Hydrogeology
- Geophysics
- Hydrology and Water Resources
- Oceanography

ISSN 2717-7696

WEB https://dergipark.org.tr/tr/pub/turkgeo

Contact cemilgezgin.jfm@gmail.com

Volume *5*
Issue *1* *March, 2025*

Contents

Research Articles;

TURKGEO
TURKISH JOURNAL OF GEOSCIENCES

ISSN: *2717-7696*
Research Article
Vol; 5, Issue; 1, pp. 1-11, 2025
DOI: *10.48053/turkgeo.1517771*
Journal homepage:
https://dergipark.org.tr/en/pub/turkgeo

Accuracy Investigation on Orthophotos Produced from Digital Aerial Imagery Recorded from Different Altitudes

Aydan Yaman*[1], Hacı Murat Yılmaz [1]

[1] *Aksaray University, Faculty of Engineering, Department of Geomatics Engineering, Aksaray, Turkey*

Keywords
Accuracy
Digital air photographs
GSD
Orthophoto map

ABSTRACT

A digital orthophoto is a topographic image that has a fixed scale like a map and on which values such as coordinates and lengths can be read, which is obtained by eliminating the errors caused by tilts and rotations in aerial images and minimizing the point shifts caused by height differences in the terrain. Digital orthophotos offer more flexible, cost-effective, and higher-quality outputs than classical methods. There is no decrease in the quality of the image as in the analog technique, and it can also be presented quickly and easily in the digital environment. The geometrical accuracy of orthophoto maps used in geomatics applications is of even greater importance. This study compared the orthophoto maps, that have a fixed scale like maps, obtained from digital aerial photographs at a GSD of 7, 15 and 25 cm in 2011 in the campus area of Aksaray University, in terms of their positional accuracy. Orthophoto mosaic images were created using "Erdas LPS" software. When the accuracy is compared, it was found that digital orthophoto maps produced at three different GSDs gave us similar results for standard techniques. It was also concluded that the positional accuracy of orthophoto maps for all three GSDs is suitable for use as a reference and basis in application areas where very high accuracy is not required, such as 3D modeling studies, highway projects, archaeological documentation, disaster management, cadastral studies, and determination of forest areas.

1. INTRODUCTION

Photogrammetry is a map production technique or science applied with measurements made on images taken from the ground with ground cameras or, more commonly used, images taken from the air with cameras placed on aircraft. The most commonly used sources in the production of data and current maps by photogrammetric method are aerial images and satellite images. However, due to various reasons, fully vertical images (aerial and satellite images) cannot be taken from airplanes and satellite systems, and the images taken have a certain degree of obliquity and rotation with the axes of the land coordinate system (X, Y, Z). In addition, due to the fact that the terrain is not perfectly flat, has various height differences, and is not perfectly parallel to the horizontal plane, the scale changes at every point of the aerial and satellite images taken, and the raw image data obtained cannot be used directly as a map (Özbalmumcu, 2007; Polido Mantas et al., 2023). The recent surge in the utilisation of photogrammetry can be attributed to the concurrent advancement of both the hardware and software for unmanned aerial vehicles (UAVs). Through the application of photogrammetry, aerial images can be captured and valuable insights can be derived from the vast quantities of data generated. Thus enabling the measurement of changes in terrain and properties over time (Rábago and Portuguez-Castro, 2023). An orthophoto is a topographic image that has a fixed scale like a map and on which values such as coordinates and lengths can be read, which is obtained by eliminating the errors caused by tilts and rotations in aerial images and minimizing the point shifts caused by height differences in the terrain (Rossi, 2004; Nikolakopoulos et al., 2023; Dev et al.,2023). Digital orthophotos are more flexible, cheaper, and provide high-quality outputs than conventional methods. There is no decrease in the quality of the image as in the analog technique, and it can also be presented quickly and easily in the

* **Corresponding Author**

*(aydanyaman@aksaray.edu.tr) ORCID ID 0000 – 0001– 8739– 066X
(hmyilmaz@aksaray.edu.tr) ORCID ID 0000-0002-9725-5792

Received: 17/07/2024; Accepted: 08/10/2024

Cite this article

Yaman, A., & Yılmaz, H.M. (2025). Accuracy Investigation on Orthophotos Produced from Digital Aerial Imagery Recorded from Different Altitudes. Turkish Journal of Geosciences 5(1), 1-11.

digital environment (Akdeniz, 2004; Zhang et al., 2023). Orthophotos with information such as map edge information, grids, elevation curves, and place names are called orthophoto maps, and the image on a single base formed by combining many orthophotos is called an orthophoto mosaic. Today, the need for up-to-date maps is increasing in every field, and orthophoto maps, which have the accuracy and precision criteria of a standard map are preferred in many application areas.

The accuracy of the orthophotos produced in the studies is very important, and there are regulations on this subject in both Turkey and European countries. In Turkey, production standards for digital photogrammetric and orthophoto map production are determined in Articles 51- 73 of LSMIPR (Large Scale Map and Map Information Production Regulation). In the directive "Accuracy Standards for Digital Geospatial Data, March 2014," put into effect by ASPRS (American Society for Photogrammetry and Remote Sensing), the location (x, y) and elevation (z) accuracies of digital orthophoto images are classified according to the method and accuracy values in obtaining these data (Yıldız et al., 2015; ASPRS, 2014).

In literature, Daramola et al., (2017) tested the geometric accuracy of digital aerial images obtained with an unmanned aerial vehicle in their study titled “Assessing the geometric accuracy of UAV-based orthophotos”. They took 669 aerial photographs at a flight altitude of 100 meters and a ground sampling distance of 3.2 cm. Then, they produced a digital elevation model and orthophotos of the study area in ArcMap software. As a result, horizontal accuracy was found to be 3.207 m and vertical accuracy was found to be 0.884 m. Jacobsen (2011), in his study named “Geometric property of large format digital camera DMC II 140”, performed test flights with 71 control points at three different ground sampling distance of 5.7 cm, 9.5 cm and 20.2 cm to analyze the accuracy of the DMC II 140 digital aerial camera. As a result, the root mean square error value was found as 0.14 µm (0.020 pixels) for 5.7 cm ground sample distance (GSD) block, 0.17 µm (0.024 pixels) for 9.5 cm GSD block and 0.25 µm (0.035 pixels) for 20.2 cm GSD block. Karasaka et al., (2017), in their study titled “Geometric analysis of digital aerial images”, in order to investigate the geometric accuracies of DMC-II 250-d and Vexcel Ultracam X digital aerial cameras, they performed flights at 10 cm and 30 cm ground sampling distances in Bursa Province and used the “Match-At” software in the evaluation of the images. As a result of the balancing process for ground control points (GCPs) and check points in each block, mean square errors were calculated and for the block with 30 cm ground sampling distance, mean square errors of GCPs were found to be below 1.0 pixels in horizontal and vertical directions, mean square errors of check points were found to be below 1.0 pixels in horizontal and vertical directions. For 10 cm GSD, mean square errors of GCPs were found to be below 1.0 pixels in horizontal and vertical directions, mean square errors of check points were found to be below 1.0 pixels in horizontal and vertical directions. The results were found to be suitable for ASPRS standards and national standards in Turkey. As a result, it was concluded that 1/5000 scale digital topographic maps can be produced using digital aerial images with a ground sampling distance of 30 cm, and 1/1000 scale digital topographic maps can be produced using digital aerial images with a ground sampling distance of 10 cm. Madani et al. (2004) investigated the geometric accuracy of the DMC aerial camera in their study. In the study, aerial images taken with the Z/I Imaging aerial camera at a scale of 1/13000 and a flight altitude of 1500 m are given as an example. In this case, a pixel size of 12 µm corresponds to a ground sampling distance of approximately 13 cm. The accuracy of the control points was found to be approximately 0.065 m horizontally and 0.010 meters vertically. When the geometry of the camera is examined, it is seen that the results can meet very high accuracy demands and can even be used in Class I studies in ASPRS standards. Spreckels et al. (2005) used a Vexcel UltraCamD digital aerial camera to capture aerial images of a coal mine in Germany. 45 GCPs were used in the study. East-west flights were performed at a scale of 1/5000 and a ground sampling distance of 10 cm, and cross flights were performed at a ground sampling distance of 8 cm. 130 aerial images were obtained for 10 cm GSD and 77 aerial images were obtained for 8 cm GSD. As a result, the root mean square errors for GCPs were found to be 2.15 cm in the x direction and 3.31 cm in the y direction. Vega et al. (2017) investigated the effects of the number of GCPs on the accuracy of orthophotos obtained with an unmanned aerial vehicle. For this purpose, 160 digital aerial images were taken at a flight altitude of 120 meters in an area of 17.64 hectares. An eight-rotor unmanned aerial vehicle and a Nikon D-3100 digital aerial camera were used in image acquisition and the flight was carried out at a ground sampling distance of 3,291 cm. Then, 9 different GCPs were combined in different ways and orthophotos were produced in the “Agisoft PhotoScan” software. As a result, when looking at the 1990 ASPRS map standards, it was seen that maps at a scale of 1/150 and a contour interval of 15 cm could be used in engineering projects for 15 GCPs and a flight altitude of 120 meters. In his study, Yıldız et al., (2015) investigated which GIS product could be used as a base for the ground sampling distances required for the use of digital orthophoto products as a base for geographic information systems, and in this context, orthophoto productions corresponding to ground sampling distances of 10 cm, 30 cm and 50 cm were carried out in the selected test area. As a result of the applications, it was seen that productions with 10 cm ground sampling distances could be used in applications where 1/1000 scale digital orthophotos would be used as a base, productions with 20 cm ground sampling distances could be used in

applications where 1/2000 scale digital orthophotos would be used as a base, and productions with 50 cm ground sampling distances could be used in applications where 1/5000 - 1/10000 scale digital orthophotos would be used as a base. In addition, in his study, he compared the accuracy of the digital terrain model with the values deemed appropriate in the EuroSDR (formerly OEEPE) directive, based on the differences between the coordinates of the control points calculated from the digital terrain model data and the real terrain coordinates, and found that the results he found were lower than these values.

This study aims to eliminate the existing geometric errors in digital aerial images with different ground sampling distances and to compare their accuracy by obtaining orthophoto mosaic images on which values such as length, angle, and area of the terrain can be measured directly and which have a fixed scale everywhere like a map. For this purpose, orthophoto mosaic images were obtained using the "Erdas LPS" software, and the location accuracy was investigated by comparing the produced maps with each other and the detail points with the points measured by GPS in the field.

1.1. Factors Ffecting the Accuracy and Quality of Digital Orthophotos

The most important factors affecting the accuracy of digital orthophotos are the scale of the input and output images, the accuracy of internal and external orientation, the distribution and accuracy of GCPs (GCPs), the accuracy of the mathematical model, the accuracy of image matching and the accuracy of the digital elevation model (Ayhan et al., 2007). Factors affecting the accuracy of orthophoto can be listed as follows:

- The quality and focal length of the camera used,
- Enlargement from photo to the scale of the final product,
- The density ratio of dispositive or the quality of the bits in the scanner pixel,
- Scanner's raw data scanning quality and geometric accuracy,
- The quality of scan samples expressed in micron or photo-scale dpi,
- Marking and coordinating the accuracy of GCPs,
- Differential verticalization methods,
- The size of the resulting pixels expressed in terrain units,
- Automatic radiometric correction after differential verticalization,
- Selection of control points,
- Variance in terrain or building that depends on camera focal length,
- The density and quality of digital elevation model data (Ayhan et al., 2007; Yılmaz, 2002).

Accuracy is an important factor in digital orthophotos. Digital orthophotos are valued to the extent that they are produced with a known accuracy. Generally, the relative accuracy of digital orthophotos depends entirely on the scale of the image. In contrast, the absolute accuracy depends largely on the quality of the GCPs, the accuracy of the digital elevation model to be used for downscaling, and the scale of the photograph (Şahin, 2013).

1.2. The Role of GCPs

GCPs are used to calculate the orientation of the sensor position at the time of image acquisition. Standard photogrammetric algorithms such as space back estimation or beam compensation are used in the calculation. The position of the sensor system is expressed in terms of six parameters: X, Y, Z, ω, φ, Ķ. These parameters are used to find the exact location of each pixel of the digital image on the ground surface (Seo et al., 2024; Pathak et al.,2024).

Another important issue is the distribution of GCPs in the image and the number of additional GCPs required for compensation. The GCPs required for orthophoto are usually obtained from ground measurements to reduce the error in orthophoto pixel positions.

Orthophoto image generation uses space back estimation to determine the correspondence between object space and image space. Therefore, the accuracy of GCPs is important for orthophoto accuracy. The absolute accuracy of the orthophoto also depends on the quality of the GCPs (Şahin, 2013).

1.3. Accuracy Criteria in Digital Orthophotos

Production standards for digital photogrammetric and orthophoto map production are determined in Articles 51- 73 of the current LSMIPR (Large Scale Map and Map Information Production Regulation).

Article 54 of the regulation, which entered into force on April 30, 2018, states that depending on the scale of the map and orthophoto to be produced, the ground sampling distance cannot be more than 30 cm if the scale is 1/5000, 20 cm if it is 1/2000, 10 cm if it is 1/1000, and 5 cm if it is 1/500.

Again, as a result of block balancing, the squared average errors of the control points should be less than ±0.75 × GSD (inclusive) in X and Y coordinates and ±1× GSD (inclusive) in Z coordinates for the map or orthophoto scale to be produced in terms of the ground sampling distance specified in Article 54 of the same regulation. Maximum differences at inspection points should be less than ±1.5 × GSD (inclusive) in X and Y coordinates and less than ±2 × GSD (inclusive) in Z coordinates.

In the European Union countries, the accuracy of the digital terrain model is obtained based on the inspection points. In the "Assessment of the Quality of Digital Terrain Models" published by EuroSDR (European Spatial Data Research), the accuracy of the digital terrain model is determined according to

the following formula (Yıldız et al., 2015; Kapnias et al., 2008);

$\sigma x,y = 0.75 \times GSD \qquad \sigma z = 0.53 \times GSD$

The σx,y, and σz values calculated from the differences between the coordinates of the control points calculated from the digital terrain model data and the actual terrain coordinates should not exceed the values found in the formula published by EuroSDR (Yıldız et al., 2015; Wolf, 1974).

EuroSDR (formerly OEEPE) is an organization established in Paris in 1953 as OEEPE in accordance with an international agreement pursuant to a proposal adopted by the Council of the Organization for Economic Cooperation in Europe. Founded in 1953, OEEPE (European Experimental Photogrammetry Research Association, Organisation Europeenne d'Etudes Photogrammetriques Experimentales) became an official member of Turkey in 1990, and the representation authority was given to the General Command of Mapping. In June 2003, with a new agreement signed in June 2003, the name of the OEEPE organization was changed to EuroSDR, which was accompanied by some technological developments.

In the directive "Accuracy Standards for Digital Geospatial Data, March 2014," put into effect by ASPRS (American Society for Photogrammetry and Remote Sensing), the location (x, y) and elevation (z) accuracies of digital orthophoto images are classified according to the method and accuracy values of obtaining these data (Yıldız et al., 2015; ASPRS, 2014).

Engineering survey-based services that require very high accuracy are grouped as Class-I, high-accuracy map-making activities (large-scale map production) as Class-II, and lower-accuracy map-making activities as Class-III. According to this grouping, the horizontal accuracy standards for digital orthophotos are presented in Table 1 (Yıldız et al., 2015).

Table 1. Horizontal accuracy standards for digital orthophotos (ASPRS,2014)

Horizontal Accuracy Data Generation Class	**Photogrammeric triangulation M.S.E. (x), M.S.E. (y)**	**Orthophoto Image Accuracy**	**GCPs M.S.E. (x), M.S.E. (y), M.S.E. (z)**
Class-I	Pixel × 1.0	Pixel × 2.0	Pixel × 0.5
Class -II	Pixel × 2.0	Pixel × 4.0	Pixel × 1.0
Class -III	Pixel × 3.0	Pixel × 6.0	Pixel × 1.5
…	…	…	…
Class -N	Pixel × N	Pixel × 2N	Pixel × 0.5N

According to Table 1, for example, in order to produce orthophotos with an accuracy of 10 cm, the point accuracies obtained at the end of photogrammetric triangulation balancing should be 5 cm or less, and the geodetic accuracies of the GCPs installed on the land for photogrammetric triangulation should be 2.5 cm or less (Yıldız et al., 2015).

Similarly, in the production of digital orthophotos by ASPRS, the correlations given in Table 2 can be calculated between location (x,y) accuracies and map scales.

Table 2. The relationship between location (x,y) accuracies and map scales in digital orthophoto production

Horizontal Accuracy Data Generation Class	**Photogrammetric triangulation M.S.E. (x), M.S.E. (y) (cm)**	**GCPs M.S.E.(x), M.S.E.(y), M.S.E. (z) (cm)**
Class -I	0.0125 × map scale	0.00625 × map scale
Class -II	0.0250 × map scale	0.01250 × map scale
Class -III	0.0375 × map scale	0.01875 × map scale
…	…	…
Class -N	N × 0.0125 × map scale	N × 0.00625 × map scale

According to Table 2, in Class-I services, it is recommended that the squared mean errors of geodetic GCPs should be less than ± 6.25 cm for 1/1000 scale studies, and the squared mean errors to be obtained at the end of photogrammetric triangulation measurements and balancing with the help of these points should be less than ± 12.5 cm (Yıldız et al., 2015).

In addition, according to international standards in large-scale map production studies, it is recommended that a-priori standard deviations (default data set) during photogrammetric triangulation balancing for photogrammetric blocks;

For GCPs;

$\sigma x,y = 0.03$ m $\qquad \sigma z = 0.05$ m

For automatically measured connecting points,

$\sigma 1 = 0.002$ mm

For manually measured connecting and GCPs,

$\sigma 1 = 0.002$ mm

Direct ground referencing system;

For GNSS values; $\sigma x, y,z = 0.10$ m

For INS values; $\sigma\omega, \varphi, \text{Ķ} = 0^{o}.010$.

It is recommended that all of these meet the criteria (Yıldız et al., 2015).

2. METHOD

The orthorectification process requires digital aerial or satellite imagery of the study area, internal

orientation parameters, external orientation elements for each image, and a sufficient number of GCPs and coordinates appropriately distributed throughout the study area.

Aksaray University campus area was selected as the study region (Figure 1).

Figure 1. Study area: Aksaray University campus area

In practice, the following GSD values were used, taking into account factors affecting the map scale, such as the scale of analog aerial photographs and scanning density.

- - 7 cm GCPs

for 1/1000 Map Production Scale (Flight Alt.; Ground Alt. +700m),

- 15 cm GSD for 1/2000 Map Production Scale (Flight Alt.; Ground Alt. +1500m),

- 25 cm GSD for 1/5000 Map Production Scale (Flight Alt.; Ground Alt. +2500m).

Flight planning was made to produce aerial images with 7, 15, and 25 cm GSD resolution, and values such as flight columns and flight heights were determined (Cankurt, 2016). In the flight planning for 7 cm ground sampling distance, 106 digital aerial images of the study area were obtained with a longitudinal overlap rate of 70% and a transverse overlap rate of 30%. In the flight planning for 15 cm ground sampling distance, 38 aerial images of the study area were obtained with a 70% longitudinal and 30% transverse overlap ratio. In the flight planning for a 25 cm ground sampling distance, 40 aerial images of the study area were obtained with 70% longitudinal and 30% transverse overlap ratio. Some of the digital aerial images taken at 7 cm ground sampling distance are given in Figure 2.

Figure 2. Examples of digital aerial images taken at 7 cm ground sampling distance

The flight plan for the 7 cm ground sampling distance is presented in Figure 3.

Figure 3. Flight planning for 7 cm ground sampling distance (Cankurt, 2016)

Flights for all three ground sampling distances are presented in Figure 4.

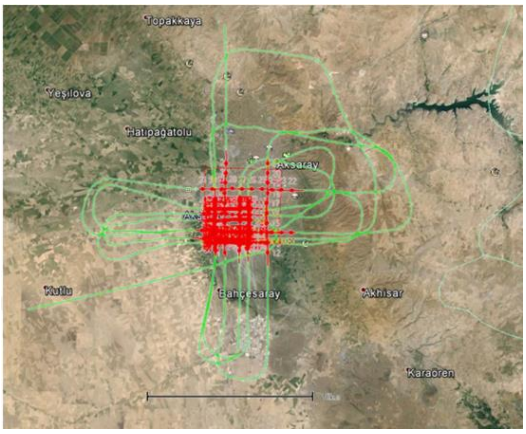

Figure 4. Flights for all three ground sampling distances (Cankurt, 2016)

In this study, it was aimed to create an orthophoto mosaic image of Aksaray University campus by using digital aerial images taken at 7 cm, 15 cm, and 25 cm ground sampling distances in 2011 and to compare the location accuracies.

The digital aerial camera Intergraph DMC was used in the study, and the calibration report is available. The internal orientation parameters were taken from there. The external orientation parameters were obtained directly from GPS/IMU during the flight.

GCPs are points that are installed on the ground so that they can be seen from aerial photographs in the study area to be flown. Since these points establish the relationship between the image coordinate system and the ground coordinate system in the rectification of images in photogrammetry and remote sensing, the accuracy and distribution of GCPs directly affect the position accuracy of the orthophotograph. In this study, 32

GCPs were installed in the study area, four Topcon GR3 GNSS receivers were used for kinematic GNSS measurements, and fixed reference points were used to determine their coordinates. The mobile kinematic measurements were performed with a Novatell OEM V2 model GNSS receiver on the UAV from which the aerial images were taken. The distribution of GCPs in the study area is shown in Figure 5.

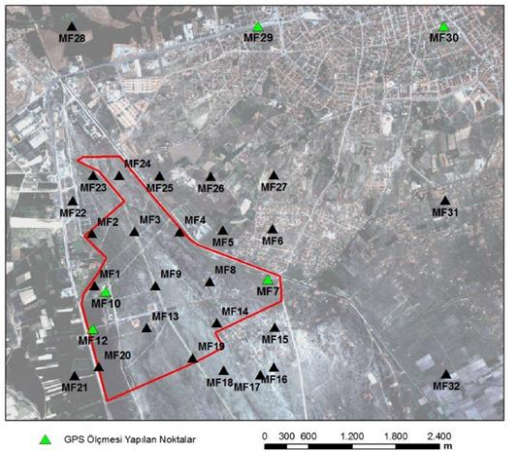

Figure 5. Distribution of GCPs within the study area

Aerial photographs were taken with 70% longitudinal and 30% transverse overlap. In the study, 32 GCPs and 24 checkpoints were used. The study aimed to produce three different orthophoto mosaics in the "Erdas LPS (2013)" software using digital aerial images taken at 7cm, 15cm, and 25 cm ground sampling distances. In the software, internal and external orientation operations were performed by adding aerial photographs. Then, the coordinate values of the GCPs installed in the field were recorded in the software, and tie points were generated. After the coordinates of the GCPs were recorded, the point distributions on the images are shown in Figure 6.

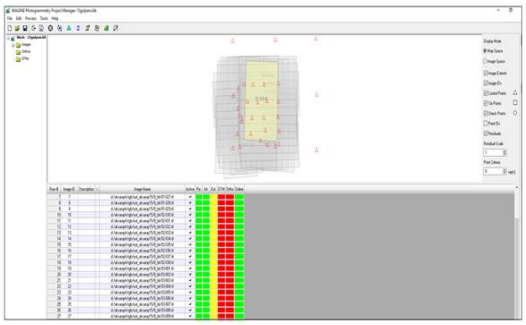

Figure 6. Distribution of GCPs on the images

All GCPs were then precisely marked on the images by opening the digital images containing each point one by one, as shown in Figure 7.

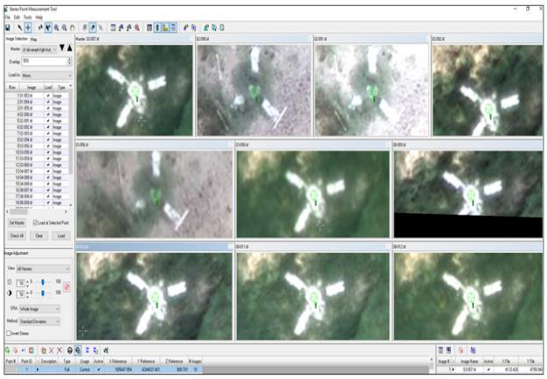

Figure 7. Marking of GCPs on aerial photographs

After this process, digital terrain model production, orthophoto production, and orthophoto mosaic production continued by balancing. The orthophoto mosaic image obtained from the study using digital aerial photographs taken with 7 cm GSD is given in Figure 8, the orthophoto mosaic image produced with digital aerial photographs taken with 15 cm GSD is given in Figure 9, and the orthophoto mosaic image obtained from digital aerial photographs taken with 25 cm GSD is given in Figure 10.

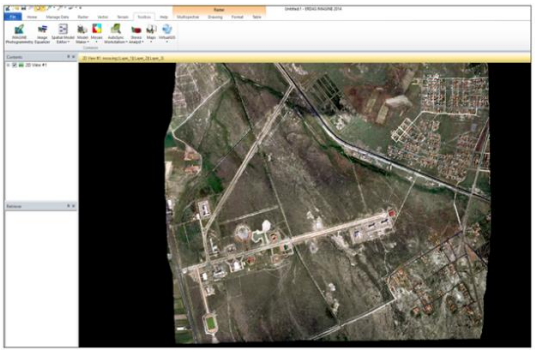

Figure 8. Orthophoto mosaic image produced using digital aerial photographs taken with 7 cm GSD

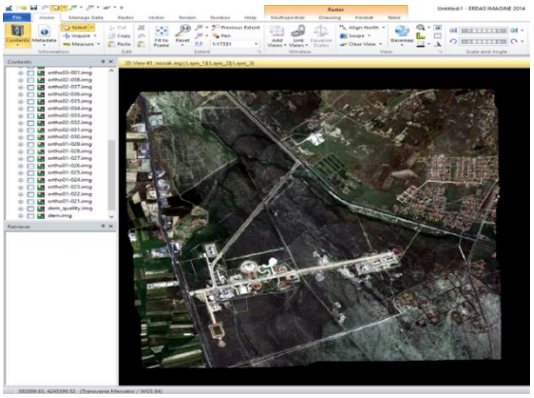

Figure 9. Orthophoto mosaic image produced using digital aerial photographs taken with 15 cm GSD

Figure 10. Orthophoto mosaic image produced using digital aerial photographs taken with 25 cm GSD

After orthophotomosaic images were produced from digital aerial images at three different ground sampling distances, the coordinates of 30 detail points distributed throughout the campus area were measured by GPS, and their coordinates were recorded, as shown in Table 3.

Table 3. GPS-measured coordinates of 30 detail points identified in the study area.

Point Number	Y (m)	X (m)
1	587435.62	4244583.21
2	587446.71	4244538.07
3	587453.84	4244529.36
4	587485.68	4244537.21
5	586483.91	4244276.08
6	586492.34	4244243.59
7	586474.48	4244238.89
8	586466.11	4244271.38
9	586455.66	4244230.83
10	586436.31	4244225.80
11	586426.31	4244264.54
12	586445.61	4244269.46
13	585937.42	4244106.20
14	585953.90	4244045.10
15	586000.84	4244057.69
16	585871.08	4244130.22
17	585939.39	4244148.02
18	585959.86	4244153.48
19	586028.83	4244171.29
20	586032.05	4244117.26
21	586039.96	4244083.82
22	586061.75	4244141.84
23	586065.89	4244127.43
24	586014.06	4244053.64
25	585896.31	4244111.97
26	585983.11	4244159.10
27	585700.07	4244645.59
28	585646.72	4244669.86
29	585662.51	4244524.76
30	587397.45	4244522.77

The general distribution of the detail points in the campus region is shown in Figure 11, divided into A, B, C, and D regions.

Figure 11. Distribution of detail points across the campus area

3. RESULTS

The coordinates of 30 detail points were measured with GPS in the field and then compared with the coordinates read on each orthophoto mosaic, and their location accuracy was calculated.

In this study, first of all, in order to test the absolute (external) accuracy of the block balancing, 24 of the 32 GCPs within the photogrammetric blocks were selected as checkpoints, and the block absolute accuracies were checked for each orthophoto mosaic produced using digital aerial images taken at three different ground sampling distances.

First of all, the coordinates of the control points measured from the model produced with 7 cm GSD were compared with the coordinates calculated by the geodetic method, and the block absolute accuracy values were found as follows;

σx = 4.52 cm, σy = 9.73 cm and σz = 9.14 cm.

Then, the coordinates of the control points measured from the model produced with 15 cm GSD were compared with the coordinates calculated by the geodetic method, and the block absolute accuracy values were found as follows;

σx = 2.47 cm, σy = 7.25 cm and σz = 8.79 cm.

After this process, the coordinates of the control points measured from the model produced with a ground sampling distance of 25 cm were compared with the coordinates calculated by the geodetic method, and the block absolute accuracy values were found as follows;

σx = 6.41 cm, σy = 9.08 cm and σz = 9.06 cm.

The values found are within the accuracy criteria given by ASPRS.

After the block absolute accuracies were calculated for all three models, the mean squared errors of ω, φ, and Ƙ values were calculated for each block in the IMU calculation. Accordingly, the orthophoto quadratic mean squared error values for 7 cm GSD are as follows;

σω = 00.0544, σφ = 00.0447 and σĸ = 00.0115.

Then, the orthophoto quadrature mean squared error values for 15 cm GSD were calculated in the IMU calculation, and the results were found as follows;

σω = 00.0479, σφ = 00.0523 and σĸ = 00.0128.

Then, the orthophoto mean squared error values for 25 cm GSD were calculated in the IMU calculation, and the results were found as follows;

σω = 00.0004, σφ = 00.0006 and σĸ = 00.0012.

The results were found to be close to or below the recommended values for IMU values in the direct ground referencing system within the a-priori standard deviations during photogrammetric triangulation balancing for photogrammetric blocks according to international standards in large-scale map production studies.

Another step in the study was to compare the coordinates of 30 detail points whose coordinates were read by GPS in the field with the coordinates read from the orthophoto mosaics obtained from the pictures taken at all three ground sampling distances and to calculate the (mp) position error for each of them.

The actual errors in the "Y" and "X" directions and the squared average errors obtained as a result of the comparison;

...are calculated from the formulas.

Here;

Yk, Xk: Classically determined point coordinates taken as reference,

Yg, Xg: Point coordinates determined by digital orthophoto,

Mx = squared mean squared error in the "x" direction,

My = squared mean squared error in the "y" direction,

Mp = position mean error and

n = Number of points (Mutluoğlu and Ceylan, 2005).

In the calculations, the position error for the orthophoto mosaic created at 7 cm GSD was found to be mp = 19.37 cm.

For the orthophoto mosaic created at 15 cm GSD, the position error was found to be mp = 19.43 cm.

For the orthophoto mosaic created at 25 cm GSD, the location error was found to be mp = 19.61 cm.

After these procedures were performed, the height (z) coordinates of the checkpoints, GCPs, and tie points on the digital terrain model produced with digital aerial photographs taken at 7 cm, 15 cm, and 25 cm ground sampling distances and the height coordinates taken from the digital terrain model. The differences between them were taken, and the squared average error was calculated. The results are as follows:

For 7 cm GSD, the squared mean error calculated from the difference between the height coordinate of the control points from the digital terrain model and the height coordinate in the field: σz = 16.58 cm,

For 7 cm GSD, the squared mean squared error of the GCPs calculated from the difference between the height coordinate from the digital terrain model and the height coordinate in the field: σz = 18.92 cm,

For 7 cm GSD, the squared mean error calculated from the difference between the height coordinate of the tie points from the digital terrain model and the height coordinate in the field: σz = 17.86 cm,

For 15 cm GSD, the squared mean squared error calculated from the difference between the height coordinate of the control points from the digital terrain model and the height coordinate in the field: σz = 11.80 cm,

For 15 cm GSD, the squared mean squared error of the GCPs calculated from the difference between the height coordinate from the digital terrain model and the height coordinate in the field: σz = 20.08 cm,

For 15 cm GSD, the squared mean squared error calculated from the difference between the height coordinate of the tie points from the digital terrain model and the height coordinate in the field: σz = 22.28 cm,

For 25 cm GSD, the squared mean squared error calculated from the difference between the height coordinate of the control points from the digital terrain model and the height coordinate in the field: σz = 23.25 cm,

For 25 cm GSD, the squared mean squared error of the GCPs calculated from the difference between the height coordinate from the digital terrain model and the height coordinate in the field: σz = 26.04 cm,

For 25 cm GSD, the squared mean squared error was calculated from the difference between the height coordinate of the tie points from the digital terrain model and the height coordinate in the field: σz = 45.67 cm.

4. CONCLUSIONS

Recently, with advances in technology, the demand for orthophoto maps has increased rapidly, considering the need for up-to-date maps, as well as speed and cost.

Orthophoto maps are highly preferred products due to the fact that they do not lose the details of the terrain, have the quality of photographs and maps, and can be easily read and interpreted by all professional groups.

In orthophoto maps, it is one of the important advantages of these products that aerial images with central projection are combined into a single image in the form of a single base with a vertical projection like a map and that values such as coordinates, distance, angle, and area can be read with sufficient accuracy on this image.

In this study, three different orthophoto mosaic images of Aksaray University campus region was produced using digital aerial images taken at 7 cm,

15 cm, and 25 cm ground sampling distances, and the location accuracy of these images was investigated. The results were compared with the values recommended in the guidelines put into effect by ASPRS (American Society for Photogrammetry and Remote Sensing).

In previous studies, Daramola et al. (2017) found the horizontal accuracy to be 3.207 m and the vertical accuracy to be 0.884 m for a flight altitude of 100 m and a GSD of 3.2 cm. Jacobsen (2011) conducted test flights with 71 GCPs at three different GSDs of 5.7 cm, 9.5 cm and 20.2 cm. As a result, the root mean square error value was found to be 0.14 µm (0.020 pixels) for the 5.7 cm GSD block, 0.17 µm (0.024 pixels) for the 9.5 cm GSD block and 0.25 µm (0.035 pixels) for the 20.2 cm GSD block. Karasaka et al., (2017) conducted flights at 10 cm and 30 cm GSDs in Bursa province and it was found that the root mean square errors of GCPs and control points for both GSDs were less than 1.0 pixels in horizontal and vertical directions. The results were found to be in accordance with ASPRS standards and national standards in Turkey. Madani et al. (2004) found the accuracy of the control points to be approximately 0.065 m horizontally and approximately 0.010 meters vertically for a GSD of 13 cm. Spreckels et al. (2005) conducted flights at 10 cm and 8 cm GSDs, and as a result, the root mean square errors for GCPs were found to be 2.15 cm in the x direction and 3.31 cm in the y direction. Vega et al. (2017), a flight was performed from a GSD of 3,291 cm, and as a result, when looking at the 1990 ASPRS map standards, it was seen that maps with a scale of 1/150 and a contour interval of 15 cm could be used in engineering projects for 15 GCP and a flight altitude of 120 meters. Yıldız et al. (2015) produced orthophotos corresponding to ground sampling distances of 10 cm, 30 cm and 50 cm, and stated that the results were lower than the values deemed appropriate in EuroSDR. The values found in the study are consistent with the results in the literature and it was observed that the block absolute accuracy values obtained from each orthophoto mosaic image, as well as the squared average errors obtained at the end of photogrammetric triangulation and block balancing of GCPs and the squared average errors obtained at the end of block balancing using the control point were found to be below the accuracy criteria given by ASPRS.

Again, the values found as a result of the squared mean squared error calculation for ω, φ, and Ƙ values in the IMU calculation were found to be close to and below the values recommended for IMU values in the direct ground referencing system within the a-priori standard deviations during photogrammetric triangulation balancing for photogrammetric blocks according to international standards in large-scale map production studies.

In addition, the accuracy of the positional data obtained from each orthophoto mosaic image was analyzed, and positional data were obtained with a mean squared error of ±19.37 cm from orthophoto mosaic obtained from digital aerial images taken with 7 cm GSD, ±19.43 cm from orthophoto mosaic obtained from digital aerial images taken with 15 cm GSD, and ±19.61 cm from orthophoto mosaic obtained from digital aerial images taken with 25 cm GSD.

Considering the horizontal accuracy standards for digital orthophotos given in Table 1 and the orthophoto image accuracies found in the study, it is recommended that the point accuracies obtained at the end of photogrammetric triangulation should be 10 cm or less in order to produce orthophotos with an accuracy of 20 cm. This condition is met for all three orthophoto mosaic images.

Although the type of the study and the accuracy expected from the result vary in the studies, it is seen that the location accuracy obtained from orthophoto images produced with 7 cm, 15 cm, and 25 cm GSD is suitable for use except for studies requiring very high accuracy (Class-I) and these digital orthophotos can be used as a base.

In addition, if the location accuracies of orthophoto mosaic images obtained from digital aerial images taken at all three ground sampling distances are also compared, in some projects, ±1m accuracy is sufficient. The production and use of digital orthophotos in projects where the accuracy of meters and above is sufficient will provide more advantages to users (Mutluoğlu and Ceylan, 2005). The location accuracies of the digital orthophoto maps produced at 7, 15, and 25 cm ground sampling distances were below 20 cm. In projects where 20 cm and above accuracy is expected, these orthophoto maps can be used. This situation provides great convenience to users in terms of advantages, costs, and production speed.

Acknowledgement

This article is produced from Aydan YAMAN's Ph.D. thesis work.

Author Contributions

Aydan Yaman: Conceptualization, Data curation, Methodology, Software, Writing-Original draft preparation. **Hacı Murat Yımaz:** Supervision, Methodology, Reviewing and Editing

Conflicts of Interest

The authors declare no conflict of interest.

REFERENCES

Akdeniz, H. (2004). Opportunities that digital orthophoto maps can provide in crisis management, *Journal of Geodesy, Geoinformation and Land Management*, (91), 13-20.

ASPRS, (2014). American society for photogrammetry and remote sensing, Accuracy Standards for Digital Geospatial Data, USA, 3-9.

Ayhan, E., Erden, Ö., & Atay, G. (2007). The effect of the digital elevation model on orthophoto production, 11th Turkish Mapping Scientific and Technical Congress, Ankara, 2-6.

Cankurt, İ. (2016). Comparison of position determination techniques in GPS/IMU systems. (Master thesis). Aksaray University, Aksaray, Turkey (in Turkish).

Daramola, O., Olaleye, J., Ajayi, O.G., & Olawuni, O., (2017). Assessing the geometric accuracy of UAV-based orthophotos. South African Journal of Geomatics, 6 (3), 395-406.

Dev, M., Veerabhadrappa, S. M., Kainthola, A., & Jha, M. K. (2023). Production of orthophoto map using mobile photogrammetry and comparative assessment of cost and accuracy with satellite imagery for corridor mapping: a case study in Manesar, Haryana, India. *Annals of GIS*, *29*(1), 163-176.

Jacobsen, K. (2011). Geometric Property of Large Format Digital Camera DMC II 140. Photogrammetrie-Fernerkundung Geoinformation, 2, 71–79.

Kapnias, D., Milenov, P. & Kay, S. (2008). Guidelines for best practice and quality checking of ortho imagery. *Joint Research Centre*, (3.0).

Karasaka, L., Karabörk, H., Güntel, A. & Esitrgen, F. (2017). Geometric analysis of digital aerial images, International Journal of Environment and Geoinformatics, 4 (1), 36-42.

Madani, M., Dörstel, C., Heipke, C. & Jacobsen,K. (2004). DMC practical experience and accuracy assessment. In Proceedings of XXth ISPRS Congress Commission II, Istanbul, Turkey. International Archives of Photogrammetry, Remote Sensing and Spatial Information Science, 35, 396–401.

Mutluoğlu, Ö. & Ceylan, A. (2005). Location accuracy and cost comparison in digital orthophoto maps, Selcuk University Journal of Engineering, Science and Technology, 20 (1), 35-42.

Nikolakopoulos, K. G., Kyriou, A., Koukouvelas, I. K., Tomaras, N., & Lyros, E. (2023). UAV, GNSS, and InSAR data analyses for landslide monitoring in a mountainous village in western Greece. *Remote Sensing*, *15*(11), 2870.

Özbalmumcu, M. (2007). Basic principles of orthophoto map production by photogrammetric method, benefits and usage areas of orthophoto, Turkish National Photogrammetry and Remote Sensing Association IV. Technical Symposium, İstanbul, 1-11.

Pathak, S., Acharya, S., Bk, S., Karn, G., & Thapa, U. (2024). UAV-based topographical mapping and accuracy assessment of orthophoto using GCP. *Mersin Photogrammetry Journal*, *6*(1), 1-8.

Pulido Mantas, T., Roveta, C., Calcinai, B., di Camillo, C. G., Gambardella, C., Gregorin, C., ... & Cerrano, C. (2023). Photogrammetry, from the land to the sea and beyond: A unifying approach to study terrestrial and marine environments. Journal of Marine Science and Engineering, 11(4), 759.

Rábago, J., & Portuguez-Castro, M. (2023). Use of drone photogrammetry as an innovative, competency-based architecture teaching process. *Drones*, *7*(3), 187.

Rossi, T.A. (2004). Application Of Digital Photogrammetric Methods İn The Of Land Cover Change On The Coastal Dunes Of Warren Dunes State Park, Berrien Country, (PhD thesis). The Michigan State University, Michigan.

Seo, D. M., Woo, H. J., Hong, W. H., Seo, H., & Na, W. J. (2024). Optimization of Number of GCPs and Placement Strategy for UAV-Based Orthophoto Production. *Applied Sciences*, *14*(8), 3163.

Spreckels, V., Fischer, C., Schlienkamp, A. & Syrek, L. (2005). Photogrammetric stereoplotting capabilities of Vexcel UltracamD digital aerial imagery, ISPRS Hannover Workshop 2005 "High-Resolution Earth Imaging for Geospatial Information", At Hannover, Germany.

Şahin, İ. (2013). Process optimization in bulk orthophoto production, (PhD thesis). Yıldız Teknik University, İstanbul, Turkey (in Turkish).

Vega, F.A., Ramirez, F.C. & Carricondo, P.M. (2017). Assessment of photogrammetric mapping accuracy based on variation GCPss number using unmanned aerial vehicle, Measurement Journal, 221-227.

Wolf, P. (1974). Elements of photogrammetry, Mc Graw Hill Publication, USA.

Yıldız, M.A., Karabörk, H. & Yıldız, F. (2015). Using digital orthophoto products as a basis for geographic information systems in spatial projects, Turkish National Photogrammetry and Remote Sensing Association VIII. Technical Symposium, Konya, 449-455.

Yılmaz, A. (2002). Accuracy research of digital elevation models produced from different sources, (PhD thesis), Yıldız Teknik University İstanbul (in Turkish).

Zhang, J., Xu, S., Zhao, Y., Sun, J., Xu, S., & Zhang, X. (2023). Aerial orthoimage generation for UAV remote sensing. *Information Fusion*, *89*, 91-120.

TURKGEO
TURKISH JOURNAL OF GEOSCIENCES

ISSN: *2717-7696*
Research Article
Vol; 5, Issue; 1, pp. 12-28, 2025
DOI: *10.48053/turkgeo.1613103*
Journal homepage:
https://dergipark.org.tr/en/pub/turkgeo

Assessment of the Performance of Sentinel-2A MSI and Landsat 9 OLI Images in Land Cover/Use Classification by Comparing Machine Learning Algorithms: A Case Study of Soma District, Turkiye

Sajaweddin Sadid[*1], **Kaan Kalkan** [2]

[1] *Eskisehir Technical University, Institute of Earth and Space Sciences, Remote Sensing and Geographic Information Systems, Eskisehir, Turkey*
[2]*TÜBİTAK Space Technologies Research Institute, Ankara, Turkey*

Keywords
Land cover
Remote sensing
Machine learning algorithms
Classification

ABSTRACT

The combination of rapid, uncontrolled population growth and economic and industrial development has significantly accelerated land use/land cover (LULC) changes. Assessing these changes is one of the most effective ways to understand and manage land transformation. The advancement of remote sensing technology and increased accessibility to satellite data have made it more feasible to produce accurate and up-to-date LULC maps through the development of classifier algorithms. This has enabled better assessment and management of ecosystem and land use changes. The main objective of this study is to evaluate the performance of four machine learning algorithms—RF, SVM, CART, and GTB—using Sentinel-2 and Landsat 9 satellite images for the Soma district of Turkiye, on the Google Earth Engine (GEE) platform. In the study, a kernel function was applied to the SVM algorithm. Downloaded satellite images were visually inspected, and Google Earth Pro images were utilized to create training and test samples. Sentinel-2 and Landsat 9 images were classified using these training data and machine learning algorithms on the GEE platform. In the evaluation of the results, an error matrix was generated for the classified images, using the test samples for validation. The evaluation showed that the overall accuracy of the SVM algorithm, using the kernel function, was 92.6% for Sentinel-2 and 87% for Landsat 9, placing it third in terms of accuracy. The GTB algorithm provided the highest overall accuracy, with 94.4% for Sentinel-2 and 88.3% for Landsat 9. The RF algorithm achieved 93.2% accuracy for Sentinel-2 and 87% for Landsat 9, matching the accuracy of SVM for Landsat 9. CART demonstrated the lowest performance, with 86.4% accuracy for Sentinel-2 and 91.4% for Landsat 9. Additionally, Sentinel-2 imagery performed better than Landsat 9 across all algorithms due to its higher spatial resolution and spectral characteristics. This study provides valuable insights for local and provincial planners, authorities, and decision-makers regarding proper land management and the production of reliable LULC maps, especially in mining regions.

1. INTRODUCTION

The dynamic process of land use/land cover change worldwide is an indispensable source of concern, signaling global environmental change. It represents one of the most remarkable regional anthropogenic degradations of the environment. At the same time, even though land is an extremely precious natural resource and has all the material wealth for mankind, the extraction of natural resources through mining activities inevitably leads to changes in land use and land cover (Garai & Narayana, 2018). In this context, knowledge of land use and land cover at various scales contributes to the study of a wide range of current and future global phenomena, including drought, flooding, erosion, and climate change.

* **Corresponding Author**

*(qarluq.sadid.2018@gmail.com) 0000-0002-0031-4531
(kalkaan@gmail.com) ORCID ID 0000-0002-2732-5425

Received: 04/01/2025; Accepted: 25/03/2025

Cite this article

Sadid, S., & Kalkan, K. (2025). Assessment of the Performance of Sentinel-2A MSI and Landsat 9 OLI Images in Land Cover/Use Classification by Comparing Machine Learning Algorithms: A Case Study of Soma District, Turkiye. Turkish Journal of Geosciences 5(1), 12-28.

Continuous and accurate analysis of land use and land cover (LULC) is an integral part of sustainable development activities in any region. Earth science and remote sensing organizations have a traditional interest in accurate and up-to-date monitoring, providing valuable data for understanding the relationships between people and their environment (Praticò et al., 2021). Detailed and accurate land cover maps are recognized as an important input in various scientific studies, such as climate change impacts on streamflow and water budgets (Sridhar et al., 2019|; Kumar et al., 2022), geomorphology (Sujatha and Sridhar, 2018; Jayappa et al., 2006), groundwater management (Xiao et al., 2022b), social information management of natural resources (Sridhar et al., 2021) and agricultural land monitoring (Sierra-Soler et al., 2015). LULC maps contribute to the control of land degradation in agriculture and watershed management in general or because of mining activities (Cihlar, 2000; Chen et al., 2020).

Remote sensing satellite imagery is one of the primary data sources that facilitates access to vast amounts of data and information for Earth observation and monitoring. Remote sensing techniques are widely used to study urban expansion, land degradation caused by mining activities, and changes in land cover. Satellites provide a variety of sensors, image resolutions, collection methods, and spatiotemporal characteristics to observe the Earth from the surface to space (Mangkhaseum and Hanazawa, 2021). Today, with tools such as Google Earth Engine (GEE), remote sensing, GIS technology, Google Earth, and machine learning algorithms, the spatial mapping of land use, land cover, and other Earth surface features can now be done more quickly and accurately (Pande, 2022).

Producing low-resolution land cover maps over large areas requires processing large volumes of data, which demands significant storage capacity, substantial processing power, and flexibility in using various approaches. These needs have been met with the release of Google Earth Engine (GEE), which makes the technology freely available to everyone (Gorelick et al., 2017). GEE provides free access to satellite imagery from sources such as Landsat, Sentinel, and MODIS.

Recently, with population growth and industrial development, mining activities have been increasing to meet energy demands, and the use of modern mining techniques and heavy equipment worldwide, especially in Turkiye, is causing significant changes in land cover, ecology, and hydrology (Garai and Narayana, 2018). In general, mining activities lead to changes in topography (Manna and Maiti, 2014) and drainage patterns (Manna and Maiti, 2016; Kříbek et al., 2023), as well as environmental impacts such as landscape alteration and degradation (Tadesse et al., 2017; Y. Shi et al., 2024), soil erosion and degradation (Xiao et al., 2022a), and broader environmental changes (Tripathi et al., 2024; Mehta et al., 2024).

As a developing country, Turkiye's energy needs are increasing daily. Consequently, to meet the demand for energy production through thermal power plants, the coal mining industry is steadily ramping up its production, driven by the reliance on coal for electricity generation. The Soma coal basin, situated in the Soma district of Manisa province, contains one of the most significant coal reserves in the country. This basin is vital for lignite coal production and contributes substantial value to the Turkish economy. It plays a critical role in fulfilling Turkiye's energy requirements and serves as the primary fuel source for thermal power plants in the region. However, sustainable mining practices and effective environmental management strategies are essential for ensuring the long-term availability of coal and safeguarding the environmental health of the basin. In this context, it is crucial to study the impact of mining on land use and land cover changes in the region to mitigate the environmental impacts of mining activities and facilitate efficient land management and decision-making processes (Wang et al., 2019).

When we examine the literature, the researcher has used various remote-sensing images for LULC classification. These studies focused on the classification and extraction of features such as cultivated land, shrubland, agriculture, bare land, and water bodies (Wang et al., 2019; Pande, 2022; Praticò et al., 2021). Lu and Weng (2007) showed that the results of land use/cover mapping depend not only on the suitability of the imagery but also on the appropriate choice of classification methods. Various classification approaches have been developed and evaluated for land use/cover assessment using remotely sensed data. Various classifiers have been used in land use/cover assessment, including unsupervised algorithms such as the ISODATA clustering algorithm or K-means, parametric supervised algorithms such as maximum likelihood (ML), and machine learning algorithms such as artificial neural networks (ANN), k-nearest Neighbors (kNN), decision trees (DT), support vector machine (SVM), random forest (RF), and Classification and Regression Trees (CART) (Friedl and Brodley, 1997; Waske and Braun, 2009; Li et al., 2014; Shao and Lunetta, 2012; Chen et al., 2020) (Oo et al., 2022; Zhao et al., 2024). Nonparametric approaches, especially machine learning-based algorithms, have received significant attention in remote sensing studies over the last decade (Thanh Noi and Kappas, 2018; Oo et al., 2022).

Many studies have been conducted to determine the best algorithm for land use/land cover classification by evaluating their performance. However, the results obtained can vary significantly. In a land cover classification study conducted by (Dixon and Candade, 2008) using Landsat TM data, SVM performed well, while Maximum Likelihood performed much worse. Moreover, previous studies

have shown that SVM outperforms traditional classification algorithms such as maximum likelihood (ML), k-nearest neighbor (kNN), and neural networks (NN) in hyperspectral remote sensing classification (Huang et al., 2002; Melgani and Bruzzone, 2004; Pal and Mather, 2005). Oo et al. (2022) compared four machine learning algorithms, namely Maximum Likelihood, Random Forest, Support Vector Machine, and CART for Land Cover Classification in Gold Mining. As a result of the study, the RF algorithm was found to have the highest accuracy. Thanh Noi and Kappas. (2018) used RF, K-Nearest Neighbor, and SVM algorithms for land cover classification. At the end of the study, SVM was found to have the highest accuracy among the three machine learning algorithms.

There is no denying that in a mining area where many human activities take place, there will be many disturbances that can change land use/land cover. In this context, it has been proven that there is a critical relationship between long-term open-cast mining activities and land use/land cover changes in the mining basin (Paraskevis et al., 2021). Vorovencii. (2024) applied Maximum Likelihood, Minimum Distance, and SVM algorithms using Landsat image series in the assessment of long-term land cover changes in the Jiului Valley mining basin in Romania. As a result of the classification, forest, residential areas, mining areas, and water bodies in the region have increased, while pasture, agricultural land, and garbage dump areas have decreased.

A review of the literature reveals a scarcity of studies that compare and evaluate the performance of machine learning algorithms utilizing Landsat and Sentinel-2 imagery, particularly in mining regions. This gap underscores the importance of comparing and assessing the effectiveness of four specific classifiers: Random Forest (RF), Support Vector Machine (SVM), Classification and Regression Trees (CART), and Gradient Boosting Trees (GBT) in the context of land use/land cover (LULC) mapping. With the growing demand for reliable LULC data derived from extensive satellite imagery, understanding the performance of various machine learning methods on widely utilized cloud-based platforms, such as Google Earth Engine (GEE), has become increasingly crucial. In this study, we employ four machine learning classifiers—RF, SVM, GBT, and CART—to systematically evaluate the performance of Landsat-9 OLI and Sentinel-2A satellite imagery for LULC classification in the Soma district of Manisa, Turkiye, from June 1 to August 30, 2023. The objective of this research is twofold: to determine which satellite imagery provides superior performance in LULC classification and to identify which of the machine learning classifiers yields the best classification results.

2. STUDY AREA

This study focuses on the Soma district, which covers a total area of 838.9 km^2. As a coal basin, the Soma district faces various environmental challenges, including mining waste, pollution of water resources, and soil contamination. Additionally, it was selected as the study area for several reasons, such as the expansion of urban areas due to the increasing population. Soma is in Manisa province in the Aegean Region of Turkiye, positioned at approximately 39°11′18″ north latitudes and 27°36′32″ east longitudes (Figure 1). As one of the most important coal basins in Turkiye, Soma attracts attention for its natural beauty and historical richness, holding both local and regional significance. Situated 100 km northeast of Izmir and 50 km from the Aegean coast, Soma's strategic location plays a vital role in its economic and cultural activities. Its proximity to Izmir and distance from the Aegean coast enhance Soma's prominence, making it a distinct and noteworthy region.

The physical environment of Soma has been drastically altered by ongoing lignite exploitation in the open coal basins to the northeast and southwest, as well as by the thermal power plant operating near the city center (Karadağ, 2006). While this change has resulted in a series of environmental problems due to mining activities and misuse, it has also significantly impacted the socio-economic structure of the city, introducing a new urban population with diverse urban life tendencies and expectations. The elevation of Soma varies between 59 m and 1209 m above sea level. The main geological formations in the area include clay, marn, and limestone, along with andesite and basalt rocks (https://eli.tki.gov.tr/soma). Due to its location under the influence of the Mediterranean climate, the average annual temperature in Soma is estimated to be between 15.3 °C and 16.1 °C, with annual precipitation totaling 554.4 mm. Soma's landscape structure and land cover dynamics exhibit complex patterns, comprising forests, agricultural lands, shrubland, open-pit coal mining activities, settlements, bare areas, and water bodies.

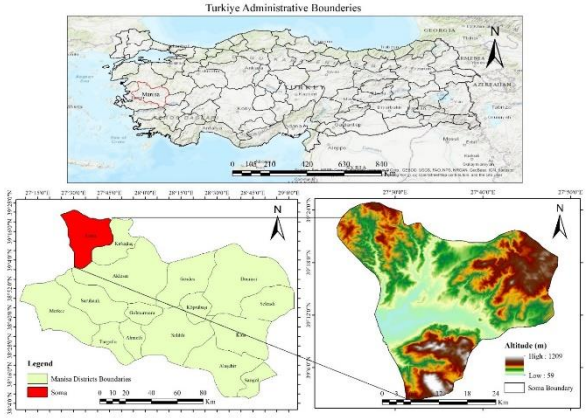

Figure 1. Geographical location of the study

3. MATERIAL and METHODS

3.1. Dataset

A vast amount of Earth observation data (EOD) from the past 40 years, including popular satellite imagery such as Sentinel, Landsat, and MODIS, as well as other geospatial data like climate and demographic information, is stored on the cloud-based Google Earth Engine (GEE) platform. Landsat and Sentinel data are accessible through GEE from the U.S. Geological Survey (USGS) and the European Space Agency (ESA). In this study, Sentinel-2 MSI and Landsat 9 OLI satellite images from 2023 were used to evaluate four machine learning classifiers for land use/land cover classification. To capture the period of vegetation growth and obtain cloud-free satellite images the months of June to August were selected and averaged. The Landsat 5 and Landsat 8 sensors have a spatial resolution of 30 meters and a swath width of 185 kilometers (http://landsat.gsfc.nasa.gov). Sentinel-2 sensors feature spatial resolutions of 10, 20, and 60 meters, depending on the spectral band, with a swath width of 290 kilometers (https://sentinel.esa.int). Table 1 below shows the characteristics of the satellite imagery.

Table 1. The primary features of Landsat-9 and Sentinel-2

Sensor	Collection	Bands	Spectral Range (μm)	Pixel Size (m)	Spectral Resolution	Radiometric Resolution (bit)	Revisit time (days)	Cloud Cover (%)
Landsat-9	Surface Reflectance Level 2, Collection 2, Tier 1	B1:Coastal/aerosol	0.433–0.453	30	11 Bands	16	16	> 5
		B2: Blue	0.450–0.515	30				
		B3: Green	0.525–0.600	30				
		B4: Red	0.630–0.680	30				
		B5: NIR	0.845–0.885	30				
		B6: SWIR1	1.560–1.660	30				
		B7: SWIR2	2.100–2.300	30				
		B8: Panchro.	0.500–0.680	15				
		B9: cirrus	1.360–1.390	30				
		B10: TIRS 1	10.30–11.30	100				
		B11: TIRS2	11.50–12.50	100				
Sentinel-2	Surface Reflectance Multi Spectral Instrument, Level 2A	B1: Coastal	0.433–0.453	60	13 Bands	12	5	> 5
		B2: Blue	0.457–0.522	10				
		B3: Green	0.542–0.577	10				
		B4: Red	0.650–0.680	10				
		B5: Red Edge	0.679–0.718	20				
		B6: Red Edge	0.732–0.747	20				
		B7: Red Edge	0.773–0.793	20				
		B8: NIR	0.784–0.899	10				
		B8A:Red Edge	0.855–0.885	20				
		B9: Water vapor	0.935–0.955	60				
		B10: Cirrus	1.36–1.39	60				
		B11: SWIR1	1.565–1.655	20				
		B12: SWIR2	2.10–2.28	20				

3.2. Image Preprocessing

In the Google Earth Engine (GEE) platform, machine learning algorithms were used comparatively to evaluate the performance of Landsat 9 OLI and Sentinel-2A MSI imagery to create a land cover/use map of the Soma district in Manisa province, Turkiye, which is the study area, for the months of June to August 2023 (Figure 2). Image preprocessing in the GEE platform is an important step that allows for image cropping, cloud masking, and the creation of topographically corrected image composites. Following image enhancement, a crucial step is to extract the normalized difference vegetation index (NDVI), normalized difference water index (NDWI), and normalized difference built-up index (NDBI), which are considered inputs for the classification algorithms. These indices are then combined with the spectral bands. Therefore, NDVI, NDWI, and NDBI are calculated based on the band values of Landsat 5, Landsat 8, and Sentinel-2 images according to the equations provided below, and the resulting maps are shown in figure 2.

The corrected Landsat and Sentinel-2 images with the lowest amount of cloud cover were used as the initial inputs for classification. The first step after importing the satellite data into Google Earth Engine (GEE) is to remove cloud shadows and cloud cover. Using a cloud mask, pixels contaminated by clouds or those with cloud-free conditions were eliminated from all available images (Mateo-García et al., 2018). In the second stage, Landsat and Sentinel data for each selected year were combined into a single image using a mean filter to create a composite image. Each pixel is assigned an average value from the entire image stack, resulting in one composite image for the entire collection. In this study, the normalized difference vegetation index (NDVI), normalized difference water index (NDWI), and normalized difference built-up index (NDBI) were calculated for the selected years and combined with the spectral bands as additional spectral features to enhance classification accuracy. NDVI is calculated using the near-infrared (NIR) and red bands (Townshend & Justice, 2007), NDWI is calculated using the green and shortwave infrared (SWIR)

bands (McFeeters, 1996), and NDBI is calculated using the SWIR and NIR bands (Zha et al., 2003), as shown in the following equations.

$$NDVI = \frac{NIR - RED}{NIR + RED} \quad (1)$$

$$NDWI = \frac{GREEN - SWIR}{GRESSN + SWIR} \quad (2)$$

$$NDBI = \frac{SWIR - NIR}{SWIR + NIR} \quad (3)$$

As a final step, the Random Forest (RF), Classification and Regression Trees (CART), Support Vector Machine (SVM), and Gradient Tree Boosting machine learning algorithms in GEE were used to train the classifiers for Landsat -9 OLI and Sentinel-2 images.

3.3. Training and Validation Sample Datasets

In this study, a set of geometric points (features) for each category (Water, Forest Area, Settlement Area, Agricultural Area, Vegetation, Bare Area, and Mining Area) was collected based on visual interpretation of the original Landsat and Sentinel-2 composite images, as well as high-resolution images from Google Earth. Training data were then generated using this collection of features for each category. This training data was divided into 80% for training the machine learning classifier models and 20% for testing to evaluate classification accuracy.

Table 2. Land cover classes are defined in this study

Class	Number of Point	Description
Water	100	Includes rivers, lakes, and other water bodies.
Forest area	107	Land dominated by trees.
Residential area	107	Areas used for residential, commercial, industrial, or mixed-use purposes.
Agriculture area	108	Includes all cultivated land and areas used for agricultural purposes.
Vegetation	100	Grassland areas including shrubs, meadows, and pastures.
Bare land	103	Typically includes soil, sand, or rock with minimal vegetation.
Mining Area	104	Designated areas for mining activities, including coal, sand, gravel pits, and other extractive industries.
Total	**729**	

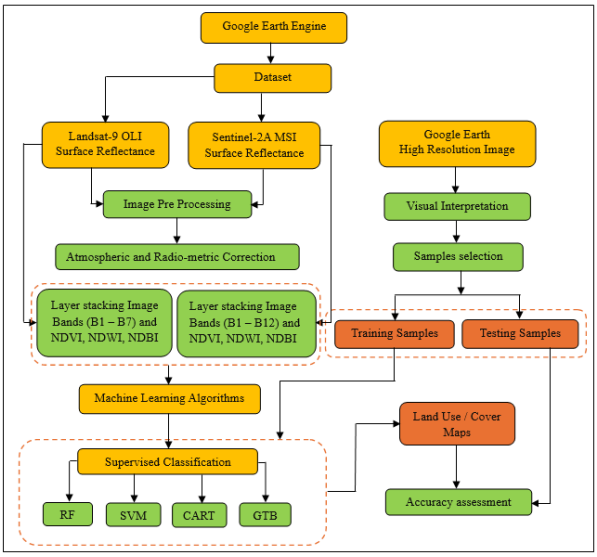

Figure 2. Flowchart for process of LULC classification within the GEE Platform

3.4. Supervised Classification Models

After collecting the training data and incorporating features that store the known class labels and predictor values, the classifiers need to be trained. The Google Earth Engine (GEE) platform offers several classifier packages for supervised classification using machine learning algorithms. However, in this study, four classifiers—Random Forest (RF), Support Vector Machine (SVM), Classification and Regression Trees (CART), and Gradient Tree Boost (GTB)—were used to evaluate the performance of Sentinel-2 and Landsat 9 data in land cover and land use classification. At this stage, the machine learning algorithms were trained using the collected training data and applied to the Landsat-9 OLI and Sentinel-2A composite image bands to produce a classified map of the study area. Below is an overview of each classifier algorithm used in this study.

Random Forest (RF): The Random Forest (RF) algorithm is rooted in the theory of bagging ensemble learning, introduced by Prof. Leo Breiman at the University of California in 1996 (Breiman, 2001). The RF algorithm has been extensively applied to solve various environmental problems and has demonstrated versatility in handling diverse data types, including satellite imagery and digital datasets (Abdullah et al., 2017). Due to its robustness in feature selection, RF is recognized as an effective and reliable supervised machine-learning technique (Xu & Cheng, 2024). to build the RF classifier model, two critical parameters are required: (1) n – the number of decision trees, commonly referred to as "trees," and (2) m – the number of attributes considered at each split, known as "trials" (Oo et al., 2022). The classification decision is made through a majority vote, where each decision tree contributes to the result based on its accuracy. The final

classification is determined by aggregating the votes from all trees in the forest. The following formula is used to determine the final classification result (Xu & Cheng, 2024).

$$H(x)=\text{voting} \sum_{i=1}^{k} I(h_i(x) = \gamma \quad (4)$$

Here, H(x) is the classification combination model; hi is the classification model of the decision tree; I() is the indicator function (this value is considered to be 1 when present in the parameter set and 0 when not present in the set) and γ represents the target variable (or output variable).

Support Vector Machine (SVM): Support Vector Machine (SVM) is a non-parametric algorithm first proposed by Vapnik and Chervonenkis (Vapnik & Chervonenkis, 1971). The SVM method constructs a hyperplane based on the largest margin between the given training sample sets and then classifies the segmented objects into recognized LULC (Land Use/Land Cover) classes. According to Knorn et al. (2009) and Shi & Yang (2015), the radial basis function (RBF) kernel of the SVM classifier is widely used in land cover classification studies and demonstrates strong performance. When implementing an SVM classifier with an RBF kernel, two key parameters need to be tuned: the optimal cost parameter (C) and the kernel width parameter (γ) (Qian et al., 2015; Ballanti et al., 2016). The C parameter controls the trade-off between allowing misclassification in the training data and creating a simpler decision boundary, thus adjusting the rigidity of the classifier. The γ parameter influences the smoothness of the class-separating hyperplane (Melgani & Bruzzone, 2004). While larger values of γ can lead to overfitting, they also affect the shape of the class-separating hyperplane, potentially impacting classification accuracy (Huang et al., 2010).

Classification and Regression Tree (CART): Breiman et al. developed the decision tree (DT) model, a widely used non-parametric method (Breiman et al., 1984). The classification and regression tree (CART) algorithm is a particularly common decision tree used for various purposes. A tree is constructed in CART through a binary iterative partitioning process, where the training sample set is split into subsets based on an attribute value test, and this process is repeated for each resulting subset (Shao & Lunetta, 2012; Oo et al., 2022). The tree-growing process concludes when further partitioning of subsets is no longer feasible. In the CART algorithm, the maximum depth of the tree is a crucial tuning parameter that determines the model's complexity. Generally, a greater depth allows the creation of a more complex tree, which may improve overall classification accuracy. However, an excessive number of nodes can lead to overfitting, where the model becomes too tailored to the training data, potentially reducing its generalization capability.

Gradient Tree Boost (GTB): Gradient Tree Boosting (GTB) is a powerful ensemble machine-learning technique used for regression and classification problems. It produces a prediction model typically in the form of an ensemble of weak prediction models using decision trees and has demonstrated significant success across a wide range of practical applications (Natekin & Knoll, 2013). However, the GTB classifier limits the complexity of individual decision trees by restricting them to weaker prediction models. The algorithm minimizes the loss function step-by-step through gradient descent optimization, improving classification accuracy by iteratively combining weak learners into a stronger ensemble of trees (Friedman, 2002). Unlike other ensemble classifiers, GTB adapts to the residuals of the regression tree at each iteration by using negative gradient loss values (Ouma et al., 2023). This method stochastically reduces the correlation between trees by generating new trees based on a selected training subset of the data.

4. RESULTS

4.1. Accuracy Assessment and Comparisons

An essential phase in all classification projects is the validation and accuracy assessment stage. This phase is a critical component of modeling and mapping, used to evaluate the effectiveness and scientific significance of the classifier models. The purpose of accuracy assessment is to compare the classified image with another data source, typically ground truth data. To assess the performance of the classifier models, confusion or error matrices are constructed by cross-referencing the classified land cover/use results with the test samples. Four commonly used metrics in remote sensing image classification—producer accuracy, user accuracy, overall accuracy, kappa coefficient—and the F1-score (equations 5–9) are used to evaluate the accuracy of the classified land cover/use (Hong et al., 2023). Producer Accuracy measures the degree of correctness and refers to the proportion of instances that truly belong to a specific class among all instances classified as that class. On the other hand, User Accuracy is the proportion of instances classified as a particular class relative to all instances that genuinely belong to that class (Ouma et al., 2023). Overall Accuracy represents the ratio of correctly classified instances to the total number of instances. The Kappa index assesses the level of agreement between the predicted and actual classes while accounting for the likelihood of correct classification occurring by random chance. Finally, the F1-measure, which is the harmonic mean of Producer and User Accuracy, is calculated to evaluate performance at both the classifier and class levels.

$$UA = \frac{K_{ii}}{K_{i+}} \quad (5)$$

$$PA = \frac{K_{jj}}{K_{j+}} \quad (6)$$

$$OA = \frac{\sum_{i=1}^{n} K_{ii}}{K_{i+}} \quad (7)$$

$$K = \frac{T \sum_{i=1}^{n} K_{ii} - \sum_{i,j=1}^{n} (K_{i+} K_{j+})}{T^2 - \sum_{i,j=1}^{n} (K_{i+} K_{j+})} \quad (8)$$

$$F1 - Score = 2 \times \frac{UA \times PA}{UA + PA} \quad (9)$$

Where PA = producer accuracy; UA = user accuracy; OA = overall accuracy; K = Kappa index; n = number of classes; Kii = number of correctly classified classes; Ki+ = i number of pixels in row and Kj+ =i number of pixels in column i; and T = number of pixels used for accuracy assessment.

4.2. Land Cover Classification

In this study, Landsat-9 OLI and Sentinel-2A satellite imagery were comparatively applied on the Google Earth Engine (GEE) platform for land cover mapping of the Soma district in Turkiye using supervised classification methods, including Random Forest (RF), Support Vector Machine (SVM), Classification and Regression Tree (CART), and Gradient Tree Boosting (GTB) algorithms. The spectral bands of Landsat-9 OLI and Sentinel-2A surface reflectance images, acquired between June 1, 2023, and August 30, 2023, were utilized for land cover classification. Due to cloud cover, the mean composite of the images within this period was used. The classification was conducted using all Near-Infrared (NIR), Visible-Near Infrared (VNIR), and Shortwave Infrared (SWIR) bands, while Thermal Infrared (TIR) bands were excluded.

Additionally, the Normalized Difference Vegetation Index (NDVI), Normalized Difference Water Index (NDWI), and Normalized Difference Built-up Index (NDBI) were calculated and included as additional bands, as they significantly enhance the accuracy of land cover classification results (Figure 3). NDVI is commonly used to assess vegetation density, with values typically ranging from -1 to +1. In this study, the NDVI values varied between -0.625 and 0.936, as shown in Figure 3.

NDWI is employed to detect the presence of water, with values generally ranging from -1 to +1; in this study, NDWI values ranged from -0.857 to 0.800. NDBI is used to identify built-up areas and typically varies between -1 and +1; in this study, NDBI values ranged from -0.583 to 0.710 (Figure 3).

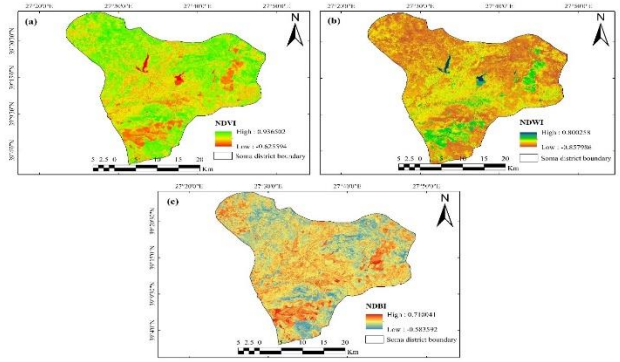

Figure 3. (a) Normalized Difference Vegetation Index, (b) Normalized Difference Water Index and (c) Normalized Difference Build up Index.

4.3. Comparison of Accuracy Analysis Results of Machine Learning Algorithms

To analyze the accuracy of land cover/use classification results from Sentinel-2 and Landsat-9 images using RF, SVM, CART, and GTB methods, five traditional metrics commonly used in remote sensing image classification were employed: producer accuracy, user accuracy, F1 score, overall accuracy, and kappa coefficient. These accuracy metrics are derived from the confusion matrix, which shows the agreement between the classified results and the reference data. Of the collected data, 80% was allocated for training and 20% for testing, while validation points were used to calculate the confusion matrix. The relevant results for Sentinel-2 and Landsat-9 images are presented in Tables 2 and 3 a,b below.

Table 3. Producer accuracy, user accuracy and F1 score values for machine learning classifier in land cover/use classification (PA = Producer Accuracy, UA = User Accuracy and F1 = F1-Score)

Class	(a) Landsat-9 OLI											
	RF			SVM			CART			GTB		
	UA	PA	F1	UA	PA	F1	UA	PA	F1	UA	PA	F1
Water	100	96	97.95	100	96	97.95	100	96	97.95	100	96	97.95
Forest area	93.33	86.66	93.33	86.66	86.66	86.66	100	86.66	92.85	87.5	93.33	90.32
Built area	80.95	76	73.91	82.60	76	79.16	89.47	68	77.27	95	76	84.44
Agriculture land	80.76	95.65	85.71	75.86	95.65	84.61	73.07	82.60	77.55	80.76	91.30	85.71
Shrubland	87.47	90.90	91.30	86.95	90.90	88.88	84.61	100	91.66	83.33	90.90	86.95
Bare land	89.47	90	87.17	100	90	94.73	88.88	80	84.21	90	90	90
Mining area	80.76	76	82.35	82.60	76	79.16	79.31	92	85.18	84	84	83.99
Class	**(b) Sentinel-2A**											
	RF			**SVM**			**CART**			**GTB**		
	UA	PA	F1	UA	PA	F1	UA	PA	F1	UA	PA	F1
Water	100	100	100	100	100	100	100	100	100	100	100	100
Forest area	100	96.29	98.11	96.29	96.29	98.11	100	96.29	100	100	96.29	100
Built area	95.45	100	95.87	87.5	100	93.33	90.9	95.23	95.2	100	90.47	100

Agriculture land	87.5	77.77	91.68	95.23	74.07	97.56	90.47	70.37	95.0	92	85.18	95.83
Shrubland	90.9	100	93.52	90.47	95	95.00	90.9	100	95.2	90.9	100	95.23
Bare land	82.6	86.36	88.92	80.76	95.45	89.36	74.07	90.9	85.1	86.95	90.9	93.02
Mining area	95.65	95.65	95.97	100	91.3	95.45	95.45	91.3	97.7	92	100	95.83

Table 3a compares the producer accuracy (PA), user accuracy (UA), and F1 score values for machine learning algorithms—Random Forest (RF), Support Vector Machine (SVM), Classification and Regression Trees (CART), and Gradient Tree Boosting (GTB)—in land cover/use classification using Landsat-9 OLI satellite images. As a result of the accuracy analysis, the water area class is classified correctly, as it has the highest values of user accuracy, producer accuracy, and F1 score across all classification algorithms. In the forest area class, the CART classifier shows the highest UA value (100), although its PA value is like those of the other methods. The RF classifier demonstrates a high F1 score (93.33) and generally provides balanced results. The SVM and GTB classifiers exhibit slightly lower performance compared to the others, with SVM showing lower UA and F1 score values.

In the residential area class, the GTB classifier achieves the highest UA (95), and its F1 score (84.44) is also the highest compared to the other methods. The CART classifier shows a lower PA (68) but maintains a high UA. Both the RF and SVM classifiers perform lower than the others, with RF exhibiting a particularly low F1 score.

In the agricultural area class, both the RF and GTB classifiers achieved the highest F1 score (85.71). SVM and CART classifiers show lower F1 scores, with CART having notably lower UA and PA values. In the shrubland class, CART achieves the highest F1 score (91.66) and PA value (100), while RF and SVM show similar results, with RF being slightly higher in terms of F1 score. The GTB classifier performed slightly lower than the others. In the bare land class, the SVM classifier outperforms the other classifiers, achieving higher UA (100), PA (90), and F1 score (94.73). In contrast, the CART classifier performs poorly, showing lower values for UA, PA, and F1. In the mining area class, the CART classifier performed better than the other classifiers, showing the highest PA (92) and F1 score (85.18) (Table 3 a,b).

When analyzing the producer accuracy (PA), user accuracy (UA), and F1 score values for land cover/use classification using Sentinel-2 satellite imagery, as presented in Table 3b, it is evident that the water area class is classified correctly, having the highest values of user accuracy, producer accuracy, and F1 score (100) across all classifiers. In the forest area class, all classifiers demonstrate high performance; however, CART and GTB excel, achieving the highest values (100) for both user accuracy and F1 score. In the residential area class, the GTB classifier attains the highest F1 score (100) and user accuracy (100), while RF shows the highest producer accuracy (100). In contrast, the SVM and CART classifiers perform worse than both RF and GTB in terms of user accuracy and F1 score. For the farmland class, SVM and CART classifiers achieve the highest F1 values of 97.56 and 95.0, respectively, but their user accuracy values of 74.07 and 70.37 are lower than those of the other classifiers. In the shrubland class, the GTB classifier outperforms the others, with user and producer accuracy and F1 values of 90.9, 100, and 95.23, respectively.

In the bare area class, the GTB classifier also surpasses the others, achieving user and producer accuracy and F1 values of 86.95, 90.9, and 93.02, respectively. In the mining area class, RF and CART classifiers yield more balanced results compared to the SVM and GTB classifiers, with F1 score values of 95.97 and 97.7, respectively (Table 3b). Overall, Landsat 9 and Sentinel 2 satellite images were classified more accurately, particularly in the water area class, where user accuracy, producer accuracy, and F1 score values were highest among the four classifiers used for land cover/use classification. Sentinel-2A satellite imagery outperforms Landsat-9 in land cover/use classification, as evidenced by its higher user accuracy, producer accuracy, and F1 score values across the four classifier methods. This superior performance may be attributed to Sentinel-2A's higher resolution and better spectral coverage.

Table 4. Confusion matrix, overall accuracy and kappa coefficient results for each classifier algorithm

(a) Confusion matrix, overall accuracy and kappa results for each classification algorithm on Landsat 9 OLI image.

ML Algorithms	Class	Water	Forest Area	Built Area	Agriculture Land	Shrubland	Bare land	Mining Area	Total
RF Classifier	Water	**24**	0	0	1	0	0	0	25
	Forest area	0	**14**	0	0	1	0	0	15
	Built area	0	0	**17**	2	0	1	5	25
	Agriculture land	0	0	0	**21**	1	1	0	23
	Shrubland	0	1	0	0	**21**	0	0	22
	Bare land	0	0	2	0	1	**17**	0	20
	Mining area	0	0	2	2	0	0	**21**	25
	Overall Accuracy	**0.870**							
	Kappa	**0.848**							
SVM Classifier	Water	**24**	0	0	1	0	0	0	25
	Forest area	0	**13**	0	0	2	0	0	15

	Built area	0	0	**19**	2	0	0	4	25
	Agriculture land	0	0	0	**22**	1	0	0	23
	Shrubland	0	2	0	0	**20**	0	0	22
	Bare land	0	0	1	1	0	**18**	0	20
	Mining area	0	0	3	3	0	0	**19**	25
	Overall Accuracy	**0.870**							
	Kappa	**0.848**							
CART Classifier	Water	**24**	0	0	0	0	0	1	25
	Forest area	0	**13**	0	0	2	0	0	15
	Built area	0	0	**17**	3	0	0	5	25
	Agriculture land	0	0	1	**19**	1	2	0	23
	Shrubland	0	0	0	0	**22**	0	0	22
	Bare land	0	0	1	2	1	**16**	0	20
	Mining area	0	0	0	2	0	0	**23**	25
	Overall Accuracy	**0.864**							
	Kappa	**0.841**							
GTB Classifier	Water	**24**	0	0	1	0	0	0	25
	Forest area	0	**14**	0	0	1	0	0	15
	Built area	0	0	**19**	2	0	0	4	25
	Agriculture land	0	0	0	**21**	1	2	0	23
	Shrubland	0	2	0	0	**20**	0	0	22
	Bare land	0	0	0	0	2	**18**	0	20
	Mining area	0	0	1	2	0	1	**21**	25
	Overall Accuracy	**0.883**							
	Kappa	**0.864**							

(b) Confusion matrix, overall accuracy and kappa results for each classification algorithm on Sentinel-2A image.

ML Algorithms	Class	Water	Forest Area	Built Area	Agriculture Land	Shrubland	Bare land	Mining Area	Total
RF Classifier	Water	**23**	0	0	0	0	0	0	23
	Forest area	0	**26**	0	0	1	0	0	27
	Built area	0	0	**21**	0	0	0	0	21
	Agriculture land	0	0	0	**21**	1	4	1	27
	Shrubland	0	0	0	0	**20**	0	0	20
	Bare land	0	0	0	3	0	**19**	0	22
	Mining area	0	0	1	0	0	0	**22**	23
	Overall Accuracy	**0.932**							
	Kappa	**0.921**							
SVM Classifier	Water	**23**	0	0	0	0	0	0	23
	Forest area	0	**26**	0	0	1	0	0	27
	Built area	0	0	**21**	0	0	0	0	21
	Agriculture land	0	0	1	**20**	1	5	0	27
	Shrubland	0	1	0	0	**19**	0	0	20
	Bare land	0	0	0	1	0	**21**	0	22
	Mining area	0	0	2	0	0	0	**21**	23
	Overall Accuracy	**0.926**							
	Kappa	**0.914**							
CART Classifier	Water	**23**	0	0	0	0	0	0	23
	Forest area	0	**26**	0	0	1	0	0	27
	Built area	0	0	**20**	0	0	0	1	21
	Agriculture land	0	0	0	**19**	1	7	0	27
	Shrubland	0	0	0	0	**20**	0	0	20
	Bare land	0	0	0	2	0	**20**	0	22
	Mining area	0	0	2	0	0	0	**21**	**23**
	Over Accuracy	**0.914**							
	Kappa	**0.899**							
GTB Classifier	Water	**23**	0	0	0	0	0	0	23
	Forest area	0	**26**	0	0	1	0	0	27
	Built area	0	0	**19**	0	0	0	2	21
	Agriculture land	0	0	0	**23**	1	3	0	27
	Shrubland	0	0	0	0	**20**	0	0	20
	Bare land	0	0	0	2	0	**20**	0	22
	Mining area	0	0	0	0	0	0	**23**	23
	Overall Accuracy	**0.944**							
	Kappa	**0.935**							

Table 4a above presents the error matrices, overall accuracy, and kappa coefficient for land cover/use classification of Landsat-9 OLI image using four different classifiers (RF, Support SVM, CART, and GTB). The GTB classifier was found to have the highest overall accuracy of 88.3% compared to the other classifiers. The CART classifier, on the other hand, has the lowest overall accuracy of 86.4%. Moreover, the GTB classifier performed better as it had the highest Kappa value of

0.864. The CART classifier, on the other hand, had the lowest Kappa value of 0.841 and performed worse than the other classifiers (Table 4a).

As shown in Table 4b, the error matrices, overall accuracy, and kappa coefficient are presented for the land cover/use classification of the Sentinel-2 image using four different classifiers: RF, SVM, CART, and GTB. The GTB classifier achieved the highest overall accuracy at 94.4%, outperforming the other classifiers. In contrast, the CART classifier recorded the lowest overall accuracy at 91.4%. Furthermore, the GTB classifier also excelled in terms of the kappa coefficient, attaining the highest value of 0.935. Conversely, the CART classifier had the lowest kappa value at 0.899, indicating its poorer performance relative to the other classifiers (Table 4b). In the classifications performed on Landsat-9 and Sentinel-2 satellite images, the GTB classifier achieved the highest overall accuracy and kappa coefficient for both images, outperforming the other methods. The CART classifier exhibited the lowest performance across both satellite images. Furthermore, Sentinel-2 provided higher overall accuracy results compared to Landsat-9. This difference can be attributed to the higher resolution and broader spectral coverage of Sentinel-2.

In this study the reference points were selected based on a stratified random sampling approach to ensure representation from all classes. However, due to the limited extent of certain land cover types, the number of points in some categories, such as water, was inherently lower. To mitigate any bias, we ensured that the selection process was proportional to the availability of each class within the study area. The number of accurate assessment points (163) was determined based on Abbas Al-Aarajy et al. (2024) while we recognize that increasing the number of points could enhance the robustness of the analysis, logistical constraints and the quality of available reference data influenced our decision to use 163 points. Nevertheless, we ensured that the selected points were well distributed and representative of the land cover classes to provide a reliable accuracy assessment.

We appreciate the reviewer's calculation regarding the number of required accuracy assessment points. In our study, the number of points was determined following standard practices in remote sensing literature. However, we agree that increasing the number of points could provide a more precise estimate of classification accuracy. In future study, it must expand the sample size to further improve the reliability of the accuracy assessment.

As a result of the study, the importance of a well-structured accuracy assessment is realized and to strengthen it, a more comprehensive review of the relevant literature will be conducted in future studies. Regarding the selection of sample points, we will examine its applicability by comparing it with other commonly used sampling strategies to provide the most reliable and unbiased accuracy assessment by considering the binomial sampling method. We will also critically evaluate and improve our methodology to address the deficiency in drawing conclusions only from existing accuracy analysis methods and to minimize possible biases and ensure the robustness of our results.

4.4. Assessment of Land Cover Change

The land cover/use classification using Landsat-9 OLI and Sentinel-2A images was conducted on the GEE platform by applying four different classifiers: RF, SVM, CART, and GTB. The classification resulted in seven classes: water, forest, settlement, agriculture, shrubland, open space, and mining area. The areas covered by each class are presented in square kilometers (km^2) and as a percentage (%) in Table 5 below.

Table 5. Comparison of the area covered by the classes

Class	(a) Landsat-9 OLI							
	RF		SVM		CART		GTB	
	Area (Km^2)	Area (%)	Area (Km^2)	Area (%)	Area (Km^2)	Area (%)	Area (Km^2)	Area (%)
Water	8.167	0.987	5.902	0.987	9.999	1.208	8.272	1.000
Forest area	117.330	14.180	133.604	14.180	128.520	15.533	111.363	13.459
Built area	52.870	6.390	48.544	6.390	65.891	7.963	42.161	5.095
Agriculture land	210.482	25.438	229.960	25.438	174.935	21.142	222.563	26.898
Shrubland	290.193	35.072	275.570	35.072	276.016	33.358	294.881	35.638
Bare land	112.070	13.544	102.353	13.544	121.607	14.697	111.995	13.535
Mining area	36.313	4.389	31.492	4.389	50.456	6.098	36.189	4.374

Class	(b) Sentinel-2A							
	RF		SVM		CART		GTB	
	Area (Km^2)	Area (%)	Area (Km^2)	Area (%)	Area (Km^2)	Area (%)	Area (Km^2)	Area (%)
Water	8.056	0.974	5.928	0.716	10.411	1.258	7.205	0.871
Forest area	163.227	19.727	161.350	19.500	164.523	19.884	158.581	19.166
Built area	53.750	6.496	47.137	5.697	41.608	5.029	47.311	5.718
Agriculture land	256.481	30.998	237.407	28.692	229.837	27.777	241.456	29.182
Shrubland	224.124	27.087	241.049	29.132	214.605	25.937	244.793	29.585
Bare land	97.004	11.724	111.298	13.451	134.689	16.278	102.751	12.418
Mining area	24.782	2.995	23.255	2.811	31.751	3.837	25.328	3.061

When analyzing the areas covered by the classes resulting from the classification of the Landsat-9 OLI image in Table 5a, it is determined that shrubland occupies the most land in the Soma region, accounting for 35.072%, 35.072%, 33.358%, and 35.638% in the RF, SVM, CART, and GTB classifiers, respectively. The agricultural area ranks second, covering 25.438%, 25.438%, 21.142%, and 26.898% in the RF, SVM, CART, and GTB classifiers, respectively. The forest area ranks third, with land cover percentages of 14.180%, 14.180%, 15.533%, and 13.459% in the RF, SVM, CART, and GTB classifiers, respectively. The bare area ranks fourth, covering 13.544%, 13.544%, 14.697%, and 13.535% of the land area, respectively. The settlement area ranks fifth, with 6.39%, 6.390%, 7.963%, and 5.095% coverage, respectively. The mining area ranks sixth, with land coverage of 4.389%, 4.389%, 6.098%, and 4.374%, respectively. The water area was found to cover the least amount of land, with 0.987%, 0.987%, 1.208%, and 1.000% in the RF, SVM, CART, and GTB classifiers, respectively (Table 5a). The GTB and CART classifiers predicted larger areas for most classes, while the RF and SVM classifiers were generally more conservative. This difference may be attributed to the varying abilities of each classifier to process spectral information and distinguish between land types.

As a result of the classification of the Sentinel-2A image presented in Table 5b, the agricultural area covers the largest percentage of land, with 30.998%, 28.692%, 27.777%, and 29.182% in the RF, SVM, CART, and GTB classifiers, respectively. Scrubland ranks second, occupying 27.087% in RF, 29.132% in SVM, 25.937% in CART, and 29.585% in GTB. The SVM and CART classifiers showed higher percentages in shrubland compared to the other classifiers. The forest area ranks third, covering 19.727% in RF, 19.500% in SVM, 19.884% in CART, and 19.166% in GTB. The bare area ranks fourth, with coverage of 11.724%, 13.451%, 16.278%, and 12.418%, respectively. Settlements ranked fifth, occupying 6.496% in RF, 5.697% in SVM, 5.029% in CART, and 5.718% in GTB. Mining areas are in sixth place, occupying 2.995% in RF, 2.811% in SVM, 3.837% in CART, and 3.061% in GTB. The water area occupies the least land, with 0.974% in RF, 0.716% in SVM, 1.258% in CART, and 0.871% in GTB. Notably, the CART classifier appears to give the highest percentage value (1.258%) for the water area (Table 5b).

When comparing the areas covered by the classes resulting from the classification of Landsat-9 OLI and Sentinel-2A images, it is observed that Landsat-9 OLI, with a spatial resolution of 30 meters, is successful in classifying larger areas. However, it may be more limited than Sentinel-2A in classifying detailed and smaller areas. Sentinel-2A, with a spatial resolution of 10-20 meters, is better able to classify smaller and finer structural differences in detail. Among the classifiers, GTB and CART predicted larger areas in both satellite images, while RF and SVM provided more limited results.

Figures 4a and 4b below show the land cover/use thematic maps for the Soma district, which was determined as the study area using four machine learning perceptron, namely RF, SVM, CART, and GTB, for the classification of Sentinel-2 and Landsat-9 images. Radial Basis Function (RBF) was used as the kernel function in the SVM classifier. RBF is a function widely used in complex and nonlinear classification problems. By transforming the data, the RBF creates more distinct boundaries between classes, thereby improving the accuracy of machine learning models.

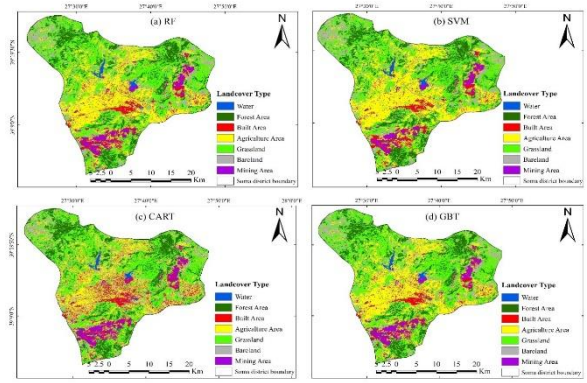

Figure 4a. Land cover/use map obtained from Landsat-9 OLI image

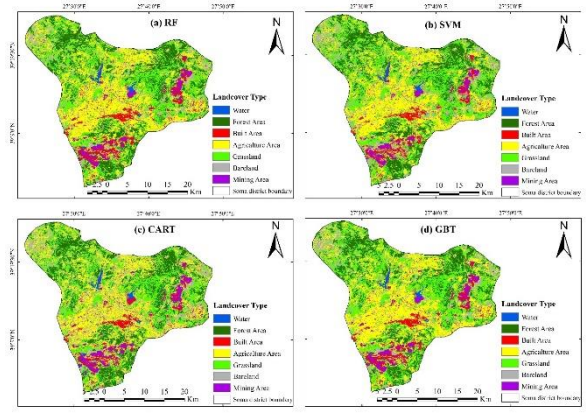

Figure 4b. Land cover/use map obtained from Sentinel-2A image

5. DISCUSSION

This study evaluated the performance of Sentinel-2 and Landsat-9 imagery for land use and land cover (LULC) mapping of coal deposits in the Soma region of Turkiye by comparing four machine learning algorithms: Random Forest (RF), Support Vector Machine (SVM), Classification and Regression Trees (CART), and Gradient Boosting Trees (GBT). Sentinel-2 and Landsat-9 images were downloaded from the Google Earth Engine (GEE) platform, where geometric and atmospheric corrections were applied. Subsequently, training samples were

collected, and machine learning algorithms were employed for LULC classification through visual interpretation and Google Earth Pro. Among these algorithms, the radial basis function (RBF), commonly used in non-parametric SVM algorithms, was utilized.

The classification results indicate that the GBT algorithm outperformed the other machine learning models in terms of overall accuracy and kappa coefficient for both Sentinel-2 and Landsat-9 imagery. Additionally, Sentinel-2 imagery exhibited slightly higher classification accuracy across all four machine learning algorithms compared to Landsat-9. Accuracy assessment metrics, including user accuracy, producer accuracy, and F1 score, were calculated from the error matrix to evaluate classification performance. The study identified seven distinct LULC classes in the Soma district: water, forest area, residential area, agricultural area, scrub area, bare area, and mining area. The water class was distinguished with the highest accuracy for both Sentinel-2 and Landsat-9 imagery. The forest area class ranked second in classification accuracy across both sensors. However, the mining area class exhibited the lowest classification accuracy, primarily due to its high spectral similarity with bare terrain and areas undergoing land degradation caused by mining activities.

The comparative analysis revealed that while advanced machine learning algorithms such as RF and SVM generally provide high classification accuracy for various terrain classes, GBT performed better in distinguishing the mining area class. This advantage is attributed to the GBT algorithm's ability to iteratively combine decision trees, allowing for improved classification performance without assuming a specific data distribution. RF and SVM, as widely recognized supervised classification algorithms, typically yield high accuracy for LULC mapping but may struggle with classes that have overlapping spectral signatures.

To contextualize the findings, the results of this study were compared with previous research on LULC classification. Shao and Lunetta (2012) applied the SVM algorithm to MODIS time series data for the Albemarle-Pamlico Estuarine System (APES) region in the United States and found that SVM outperformed neural networks (NN) and CART, achieving an overall accuracy of 77-80%. Similarly, Zhao et al. (2024) compared RF, SVM, and CART for LULC assessment in Mardan, Pakistan, using Sentinel-2 imagery, reporting overall accuracy values of 96.25%, 97%, and 98.68%, respectively, with CART performing best. Thanh Noi and Kappas (2018) evaluated RF, k-nearest neighbor (kNN), and SVM in Vietnam's Red River Delta, finding that SVM consistently achieved the highest accuracy, ranging from 90% to 95%. Other studies, such as those by Ghayour et al. (2021) and Talukdar et al. (2020), further corroborate the effectiveness of machine learning algorithms for LULC classification, with RF and SVM consistently yielding high accuracy in various geographic settings.

The performance of machine learning algorithms in classification studies is influenced by both satellite data and the characteristics of the study area. Decision tree-based models, such as CART, are prone to overfitting and are highly sensitive to variations in training datasets (Prasad et al., 2006). SVM algorithms, while computationally efficient in high-dimensional spaces, often require extensive fine-tuning and can be challenging to interpret (Huang et al., 2010). The findings of this study align with previous research, confirming that supervised classification algorithms such as RF, SVM, CART, and GBT provide reliable and high-accuracy results for Sentinel-2 and Landsat-9 imagery. Notably, the GBT algorithm demonstrated superior classification performance, particularly for the mining area class, which is often difficult to distinguish from residential and bare land classes.

This study also highlights environmental changes in the Soma region, particularly the decline in green areas due to expanding mining activities. These findings emphasize the need for effective land management strategies to mitigate the environmental impacts of mining. Sustainable land use policies should consider factors such as forest quality, vegetation cover, climate change, and human activities to ensure ecological balance and minimize land degradation.

Despite the study's contributions, certain limitations should be acknowledged. The classification accuracy of some LULC classes, particularly mining areas, was lower due to their spectral similarity with other land cover types. This challenge underscores the difficulty of distinguishing land cover categories with overlapping spectral signatures, even with advanced machine learning algorithms. Additionally, the study relied on a limited number of accuracy assessment points (163), which may have introduced bias, especially for underrepresented classes such as water. While stratified random sampling was used to ensure proportional representation, increasing the sample size could enhance result generalizability. Furthermore, since this study focused on a single region (Soma), its findings may not be directly applicable to other geographic locations with distinct LULC characteristics. Future studies should address these limitations by incorporating larger sample sizes, exploring additional spectral indices, and testing the methodology in diverse environments to enhance robustness and applicability.

Overall, this study provides valuable insights for local and regional land management authorities by demonstrating the efficacy of machine learning algorithms in LULC mapping. The findings contribute to the development of more accurate land classification techniques, ultimately aiding policymakers and researchers in making informed decisions regarding sustainable land management.

Future research should focus on refining classification methodologies, integrating additional data sources, and leveraging advanced remote sensing techniques to improve LULC mapping accuracy.

6. CONCLUSIONS

This study evaluated the performance of four supervised machine learning algorithms—Random Forest (RF), Support Vector Machine (SVM), Classification and Regression Trees (CART), and Gradient Boosting Trees (GBT)for Land Use Land Cover (LULC) classification using Sentinel-2 and Landsat 9 imagery on the Google Earth Engine (GEE) platform. Additionally, NDVI, NDWI, and NDBI indices were incorporated into the classification process to enhance class separation. The radial basis function (RBF) kernel was applied with SVM to assess its impact on classification accuracy.

The accuracy assessment results indicate that the GBT algorithm achieved the highest overall classification performance for both Sentinel-2 and Landsat 9 images, followed closely by RF. The SVM algorithm with the RBF kernel showed overall accuracy rates of 92.6% for Sentinel-2 and 87% for Landsat 9, performing better than CART but slightly lower than RF and GBT. Sentinel-2 imagery consistently outperformed Landsat 9 in class separability, likely due to its higher spatial resolution and spectral characteristics. The classification performance was further evaluated based on user accuracy and producer accuracy, revealing that the water class had 100% user accuracy across all algorithms. However, spectral similarity between certain classes, such as mining areas and bare land, led to reduced user accuracy in some cases, ranging from 80% to 95%.

To address this spectral similarity issue, future research should explore additional spectral indices or feature selection methods to improve class distinction. While NDVI, NDWI, and NDBI were used in this study, additional indices—such as soil-adjusted vegetation index (SAVI), built-up indices, or texture-based features—could be investigated to enhance classification accuracy. Moreover, the effectiveness of these indices should be systematically compared to determining their impact on resolving class confusion.

This study contributes to the literature by integrating multiple machine learning algorithms and satellite data sources while analyzing classification challenges in a complex LULC setting. Future studies should further assess classification performance under varying geomorphic and environmental conditions, incorporating additional datasets to refine classification methodologies. Developing more accurate and adaptable classification approaches will support reliable LULC mapping, which is essential for effective land management and policymaking. To overcome the limitations identified in this study, future research should focus on increasing the sample size for accuracy assessment to enhance the robustness of the results. Additionally, a comprehensive review of sampling strategies, including the binomial sampling method, should be conducted to ensure a more reliable and unbiased accuracy assessment.

Author Contributions

Sajaweddin Sadid: Conceptualization, Methodology, Software, Visualization, Writing- Original draft preparation. **Kaan Kalkan:** Data curation, Writing- Original draft preparation. Visualization, Supervision, Writing- Reviewing and Editing.

Conflicts of Interest

It has been declared that no conflicts of interest exist. The authors declare that no funding was received for this study.

REFERENCES

Abdullah, A. Y., Masrur, A., Sarfaraz, M., & Adnan, G. (2017). Spatio-Temporal Patterns of Land Use / Land Cover Change in the Heterogeneous Coastal Region of Bangladesh between 1990 and 2017. *Remote Sensing*, *11*(790), 1–26. https://doi.org/10.3390/rs11070790

Ahmed A. Zaeen, Khaleel I. Abood, Khalid H. Abbas Al-Aarajy *(2024)* Supervised Classification Accuracy Assessment Using Remote Sensing and Geographic Information System. *TEM Journal 13(1) 396-403*

Ballanti, L., Blesius, L., Hines, E., & Kruse, B. (2016). Tree Species Classification Using Hyperspectral Imagery : A Comparison of Two Classifiers. *Remote Sensing*, *8*(445), 1–18. https://doi.org/10.3390/rs8060445

Breiman, L., Frıedman, J. H., Olshen, R. A., & Stone, C. J. (1984). *Classification and Regression Tree*. Wadsworth & Brooks.

Chen, W., Li, X., & Wang, L. (2020). Fine land cover classification in an open pit mining area using optimized support vector machine and world view-3 imagery. *Remote Sensing*, *12*(1), 12–14. https://doi.org/10.3390/RS12010082

Cihlar, J. (2000). Land cover mapping of large areas from satellites: Status and research priorities. *International Journal of Remote Sensing*, *21*(6–7), 1093–1114. https://doi.org/10.1080/014311600210092

Dixon, B., & Candade, N. (2008). Multispectral landuse classification using neural networks and support vector machines: One or the other, or both? *International Journal of Remote*

Sensing, *29*(4), 1185–1206. https://doi.org/10.1080/01431160701294661

Friedl, M. A., & Brodley, C. E. (1997). Decision Tree Classification of land cover from remote sensig data. *Remote Sens. Envıron.*, *61*, 399–409.

Garai, D., & Narayana, A. C. (2018). Land use/land cover changes in the mining area of Godavari coal fields of southern India. *Egyptian Journal of Remote Sensing and Space Science*, *21*(3), 375–381.https://doi.org/10.1016/j.ejrs.2018.01.002

Ghayour, L., Neshat, A., Paryani, S., Shahabi, H., Shirzadi, A., Chen, W., Al-Ansari, N., Geertsema, M., Amiri, M. P., Gholamnia, M., Dou, J., & Ahmad, A. (2021). Performance evaluation of sentinel-2 and landsat 8 OLI data for land cover/use classification using a comparison between machine learning algorithms. *Remote Sensing*, *13*(7). https://doi.org/10.3390/rs13071349

Gorelick, N., Hancher, M., Dixon, M., Ilyushchenko, S., Thau, D., & Moore, R. (2017). Google Earth Engine: Planetary-scale geospatial analysis for everyone. *Remote Sensing of Environment*, *202*, 18–27. https://doi.org/10.1016/j.rse.2017.06.031

Hong, F., He, G., Wang, G., Zhang, Z., & Peng, Y. (2023). Monitoring of Land Cover and Vegetation Changes in Juhugeng Coal Mining Area Based on Multi-Source Remote Sensing Data. *Remote Sensing*, *15*(13). https://doi.org/10.3390/rs15133439

Huang, C., Davis, L. S., & Townshend, J. R. G. (2010). An assessment of support vector machines for land cover classification. *International Journal of Remote Sensing ISSN:*, *23*(4), 725–749. https://doi.org/10.1080/01431160110040323

Jayappa, K. S., Mitra, D., & Mishra, A. K. (2006). Coastal geomorphological and land-use and land-cover study of Sagar Island, Bay of Bengal (India) using remotely sensed data. *International Journal of Remote Sensing*, *27*(17), 3671–3682. https://doi.org/10.1080/01431160500500375

Karadağ, A. (2006). Linyit işletmeleri ve termik santralin ardından Somada değişen çevre, kent ve kimlik. *Ege Coğrafya Dergisi*, *15*(2006), 31–50.

Knorn, J., Rabe, A., Radeloff, V. C., Kuemmerle, T., Kozak, J., & Hostert, P. (2009). Remote Sensing of Environment Land cover mapping of large areas using chain classi fi cation of neighboring Landsat satellite images. *Remote Sensing of Environment*, *113*(5), 957–964. https://doi.org/10.1016/j.rse.2009.01.010

Kříbek, B., Nyambe, I., Sracek, O., Mihaljevič, M., & Knésl, I. (2023). Impact of Mining and Ore Processing on Soil, Drainage and Vegetation in the Zambian Copperbelt Mining Districts: A Review. *Minerals*, *13*(3). https://doi.org/10.3390/min13030384

Kumar, M., Denis, D. M., Kundu, A., Joshi, N., & Suryavanshi, S. (2022). Understanding land use/land cover and climate change impacts on hydrological components of Usri watershed, India. *Applied Water Science*, *12*(3), 1–14. https://doi.org/10.1007/s13201-021-01547-6

Leo Breiman. (2001). Random Forests. *Machine Learning*, *45*, 5–32. https://doi.org/10.1007/978-3-030-62008-0_35

Li, C., Wang, J., Wang, L., Hu, L., & Gong, P. (2014). Comparison of classification algorithms and training sample sizes in urban land classification with landsat thematic mapper imagery. *Remote Sensing*, *6*(2), 964–983. https://doi.org/10.3390/rs6020964

Lu, D., & Weng, Q. (2007). A survey of image classification methods and techniques for improving classification performance. *International Journal of Remote Sensing*, *28*(5), 823–870. https://doi.org/10.1080/01431160600746456

Mangkhaseum, S., & Hanazawa, A. (2021). Comparison of Machine Learning Classifiers for Land Cover Changes using Google Earth Engine. *Proceedings of the 2021 IEEE International Conference on Aerospace Electronics and Remote Sensing Technology, ICARES 2021*, 1–7. https://doi.org/10.1109/ICARES53960.2021.9665186

Manna, A., & Maiti, R. (2014). Opencast Coal Mining Induced Defaced Topography of Raniganj Coalfield in India - Remote Sensing and GIS Based Analysis. *Journal of the Indian Society of Remote Sensing*, *42*(4), 755–764. https://doi.org/10.1007/s12524-014-0363-y

Manna, A., & Maiti, R. (2016). Alteration of Surface Water Hydrology by Opencast Mining in the Raniganj Coalfield Area, India. *Mine Water and the Environment*, *35*(2), 156–167. https://doi.org/10.1007/s10230-015-0342-8

Mateo-García, G., Gómez-Chova, L., Amorós-López, J., Muñoz-Marí, J., & Camps-Valls, G. (2018).

Multitemporal Cloud Masking in the Google Earth Engine. *Remote Sensing*, *10*(1079), 2–18. https://doi.org/10.3390/rs10071079

McFEETERS, S. K. (1996). International Journal of Remote Sensing The use of the Normalized Difference Water Index (NDWI) in the delineation of open water features. *International Journal of Remote Sensing*, *17*(7), 1425-1432.

Mehta, S. A., Ashish, Solanki, M., & Seth, A. (2024). A Characterization of Land-use Changes in the Proximity of Mining Sites in India. *ACM Journal on Computing and Sustainable Societies*, *2*(1), 1–23. https://doi.org/10.1145/3624774

Melgani, F., & Bruzzone, L. (2004a). *Classification of Hyperspectral Remote Sensing Image With Support Vector Machines* (Vol. 42, Issue August, pp. 1778–1790).

Melgani, F., & Bruzzone, L. (2004b). Classification of Hyperspectral Remote Sensing Images With Support Vector Machines. *IEEE Transactıons On Geoscıence And Remote Sensıng*, *42*(8), 1778–1790.

Oo, T. K., Arunrat, N., Sereenonchai, S., Ussawarujikulchai, A., Chareonwong, U., & Nutmagul, W. (2022). Comparing Four Machine Learning Algorithms for Land Cover Classification in Gold Mining: A Case Study of Kyaukpahto Gold Mine, Northern Myanmar. *Sustainability (Switzerland)*, *14*(17). https://doi.org/10.3390/su141710754

Ouma, Y. O., Keitsile, A., Nkwae, B., Odirile, P., Moalafhi, D., & Qi, J. (2023). Urban land-use classification using machine learning classifiers: comparative evaluation and post-classification multi-feature fusion approach. *European Journal of Remote Sensing*, *56*(1). https://doi.org/10.1080/22797254.2023.2173659

Pal, M., & Mather, P. M. (2005). Support vector machines for classification in remote sensing. *International Journal of Remote Sensing*, *26*(5), 1007–1011. https://doi.org/10.1080/01431160512331314083

Pande, C. B. (2022). Land use/land cover and change detection mapping in Rahuri watershed area (MS), India using the google earth engine and machine learning approach. *Geocarto International*, *37*(26), 13860–13880. https://doi.org/10.1080/10106049.2022.2086622

Paraskevis, N., Servou, A., Roumpos, C., & Pavloudakis, F. (2021). Spatiotemporal interactions between surface coal mining and land cover and use changes. *Journal of Sustainable Mining*, *20*(2), 72–89. https://doi.org/10.46873/2300-3960.1053

Praticò, S., Solano, F., Di Fazio, S., & Modica, G. (2021). Machine learning classification of mediterranean forest habitats in google earth engine based on seasonal sentinel-2 time-series and input image composition optimisation. *Remote Sensing*, *13*(4), 1–28. https://doi.org/10.3390/rs13040586

Qian, Y., Zhou, W., Yan, J., Li, W., & Han, L. (2015). Comparing Machine Learning Classifiers for Object-Based Land Cover Classification Using Very High Resolution Imagery. *Remote Sensing*, *7*, 153–168. https://doi.org/10.3390/rs70100153

Shao, Y., & Lunetta, R. S. (2012). Comparison of support vector machine, neural network, and CART algorithms for the land-cover classification using limited training data points. *ISPRS Journal of Photogrammetry and Remote Sensing*, *70*, 78–87. https://doi.org/10.1016/j.isprsjprs.2012.04.001

Shi, D., & Yang, X. (2015). Support Vector Machines for Land Cover Mapping from Remote Sensor Imagery. In *Monitoring and Modeling of Global Changes: A Geomatics Perspective* (pp. 265–279). Springer.

Shi, Y., Fan, X., Ding, X., & Sun, M. (2024). An Assessment of Ecological Sensitivity and Landscape Pattern in Abandoned Mining Land. *Sustainability (Switzerland)*, *16*(3). https://doi.org/10.3390/su16031105

Sierra-Soler, A., Adamowski, J., Qi, Z., Saadat, H., & Pingale, S. (2015). High accuracy Land Use Land Cover (LULC) maps for detecting agricultural drought effects in rainfed agro-ecosystems in central Mexico. *Journal of Water and Land Development*, *26*(1), 19–35. https://doi.org/10.1515/jwld-2015-0014

Sridhar, V., Ali, S. A., & Sample, D. J. (2021). Systems analysis of coupled natural and human processes in the mekong river basin. *Hydrology*, *8*(3), 1–20. https://doi.org/10.3390/hydrology8030140

Sridhar, V., Kang, H., & Ali, S. A. (2019). Human-induced alterations to land use and climate and their responses for hydrology and water management in the Mekong River Basin. *Water*

(Switzerland), *11*(6). https://doi.org/10.3390/w11061307

Sujatha, E. R., & Sridhar, V. (2018). Spatial prediction of erosion risk of a small mountainous watershed using RUSLE: A case-study of the palar sub-watershed in Kodaikanal, South India. *Water (Switzerland)*, *10*(11), 1–17. https://doi.org/10.3390/w10111608

Tadesse, L., Suryabhagavan, K. V., Sridhar, G., & Legesse, G. (2017). Land use and land cover changes and Soil erosion in Yezat Watershed, North Western Ethiopia. *International Soil and Water Conservation Research*, *5*(2), 85–94. https://doi.org/10.1016/j.iswcr.2017.05.004

Talukdar, S., Singha, P., Mahato, S., & Pal, S. (2020). *Land-Use Land-Cover Classification by Machine Learning Classifiers for Satellite Observations—A Review*.

Thanh Noi, P., & Kappas, M. (2018). Comparison of Random Forest, k-Nearest Neighbor, and Support Vector Machine Classifiers for Land Cover Classification Using Sentinel-2 Imagery. *Sensors (Basel, Switzerland)*, *18*(1). https://doi.org/10.3390/s18010018

Townshend, J. R. G., & Justice, C. O. (2007). International Journal of Remote Sensing Analysis of the dynamics of African vegetation using the normalized difference vegetation index. *International Journal of Remote Sensing*, *7*(11), 1435–1445. https://doi.org/10.1080/01431168608948946

Tripathi, A. K., Aruna, M., Parida, S., Nandan, D., Elumalai, P. V., Prakash, E., Isaac JoshuaRamesh Lalvani, J. S. C., & Rao, K. S. (2024). Integrated smart dust monitoring and prediction system for surface mine sites using IoT and machine learning techniques. *Scientific Reports*, *14*(1), 1–12. https://doi.org/10.1038/s41598-024-58021-x

Vapnik, V. N., & Chervonenkis, A. Y. (1971). On the Uniform Convergence of Relative Frequencies of Events to Their Probabilities. In *Theory of Probability and Its Applications* (pp. 264–280). Springer International Publishing Switzerland. https://doi.org/10.1007/978-3-319-21852-6

Vorovencii, I. (2024). Long-term land cover changes assessment in the Jiului Valley mining basin in Romania. *Frontiers in Environmental Science*, *12*(January), 1–23. https://doi.org/10.3389/fenvs.2024.1320009

Wang, L., Jia, Y., Yao, Y., & Xu, D. (2019). Accuracy assessment of land use classification using support vector machine and neural network for coal mining area of Hegang city, China. *Nature Environment and Pollution Technology*, *18*(1), 335–341.

Waske, B., & Braun, M. (2009). Classifier ensembles for land cover mapping using multitemporal SAR imagery. *ISPRS Journal of Photogrammetry and Remote Sensing*, *64*(5), 450–457. https://doi.org/10.1016/j.isprsjprs.2009.01.003

Xiao, W., Ren, H., Sui, T., Zhang, H., Zhao, Y., & Hu, Z. (2022a). A drone- and field-based investigation of the land degradation and soil erosion at an opencast coal mine dump after 5 years' evolution of natural processes. *International Journal of Coal Science and Technology*, *9*(1). https://doi.org/10.1007/s40789-022-00513-0

Xiao, Y., Hao, Q., Zhang, Y., Zhu, Y., Yin, S., Qin, L., & Li, X. (2022b). Investigating sources, driving forces and potential health risks of nitrate and fluoride in groundwater of a typical alluvial fan plain. *Science of the Total Environment*, *802*, 149909. https://doi.org/10.1016/j.scitotenv.2021.149909

Xu, H., & Cheng, W. (2024). Landscape Analysis and Ecological Risk Assessment during 1995–2020 Based on Land Utilization/Land Coverage (LULC) and Random Forest: A Case Study of the Fushun Open-Pit Coal Area in Liaoning, China. *Sustainability*, *16*(6), 2442. https://doi.org/10.3390/su16062442

Zha, Y., Gao, J., & Ni, S. (2003). International Journal of Remote Sensing Use of normalized difference built-up index in automatically mapping urban areas from TM imagery. *International Journal of Remote Sensing*, *24*(3), 583–594.

Zhao, Z., Islam, F., Waseem, L. A., Tariq, A., Nawaz, M., Islam, I. U., Bibi, T., Rehman, N. U., Ahmad, W., Aslam, R. W., Raza, D., & Hatamleh, W. A. (2024). Comparison of Three Machine Learning Algorithms Using Google Earth Engine for Land Use Land Cover Classification. *Rangeland Ecology and Management*, *92*, 129–137. https://doi.org/10.1016/j.rama.2023.10.007